ADVANCED MATERIALS
www.advmat.de

Deciphering the Quantitative Relationship Between the Photocatalytic Activity and the Built-In Electric Field of Heterojunction

Chengwei Qiu, Jinni Shen, Haifeng Li, Yuhua Zhong, Jianhan Lin, Qing Wu, Dongmiao Li, Bing Wang, Ying Wang, Xuxu Wang, Xianzhi Fu, and Zizhong Zhang**

The principle of heterojunction in physics has been extensively referenced in heterogeneous photocatalysis, but it appears to have been utilized qualitatively more as a concept than as a method. The reason is that the quantitative correlation between the intensity of the built-in electric field (BIEF) and photocatalytic activity has not been established, primarily due to the challenges in directly measuring the BIEF of nanosized photocatalysts. To address this, both powder-type and single-crystal-type SiC@WO_{3-x}-T heterostructures are prepared to quantitatively investigate the dependence of photocatalytic CO_2 reduction activities on BIEF intensity. A strong linear correlation between the effective photoelectron number (N_{EPN}) for CO_2 reduction and the BIEF intensity is revealed for the first time. Specifically, N_{EPN} increases by 0.25 µmol g^{-1} when V_{bi} (built-in potential) increases by 1 kV for the powder sample. In contrast, for the single-crystal sample, N_{EPN} rises by 0.16 µmol with a 1 kV cm^{-1} increase in E_{bi} (built-in electric field). This study not only bridges a critical gap in heterojunction photocatalysis research but also demonstrates a method to amplify the built-in electric field by engineering the interface species, thereby enhancing the photocatalytic performance.

1. Introduction

Improving the efficiency of photocatalysis has always been a central challenge for the photocatalysis community,[1–2] necessitating a deeper understanding of the structure-activity relationship and the photocatalytic reaction mechanism. The initial step in photocatalysis involves light-induced charge separation and subsequent migration of carriers to the photocatalyst surface, which serves as a critical entry point for improving photocatalysis efficiency.[3] Constructing heterojunctions between dissimilar semiconductors is widely recognized as an effective strategy to promote the separation and migration of the photogenerated electrons and holes – a common limitation in single-component or single-phase photocatalysts. This approach has broad applicability across various photocatalytic processes, including water splitting, artificial photosynthesis, and the degradation of pollutants.[4–8] However, despite its conceptual prominence, the heterojunction strategy is often applied more as a general notion than as a practical design guideline. This limitation arises from the lack of a quantitative description of the relationship between heterojunction parameters and photocatalytic activity.[9]

The heterojunction effect is a well-defined phenomenon in semiconductor physics, and the built-in electric field (BIEF) of heterojunctions is widely acknowledged as a key factor influencing the behavior of composite semiconductor materials. Conceptually, the BIEF is formed spontaneously at the intimate contact interface between the two semiconductor components with different Fermi energy levels. In bulk heterojunction structures, both the direction and intensity of BIEF can be determined experimentally or calculated theoretically.[10,11] The mechanism of BIEF has been widely utilized as important evidence for the accurate design of electronic devices, including semiconductor lasers, solar cells, transistors, and LED lights.[10] However, for powdered composite semiconductor photocatalysts, which are typically nanostructured materials, there is currently no simple and reliable experimental or theoretical method to determine their BIEF intensity, despite several proposed models.[12–16] Most importantly, the quantitative correlation between photocatalytic activity and BIEF intensity has not been reported.[17,18] Understanding this correlation is crucial for explaining performance differences among heterojunction photocatalysts and for the accurate design and synthesis of optimized heterostructures.[3,19]

Silicon carbide (SiC) is a classic semiconductor material featuring a moderate bandgap, which enables broad absorption of solar light, along with band alignments suitable for both CO_2 reduction to various C_1 compounds and water oxidation to O_2.[20]

C. Qiu, J. Shen, H. Li, Y. Zhong, J. Lin, Q. Wu, D. Li, B. Wang, Y. Wang, X. Wang, X. Fu, Z. Zhang
State Key Lab of Photocatalysis on Energy and Environment, College of Chemistry
Fuzhou University
Fuzhou 350116, P. R. China
E-mail: t15067@fzu.edu.cn; z.zhang@fzu.edu.cn

The ORCID identification number(s) for the author(s) of this article can be found under https://doi.org/10.1002/adma.202505900

DOI: 10.1002/adma.202505900

However, pure SiC exhibits limited photocatalytic activity for CO_2 reduction with H_2O due to several inherent limitations: i) its valence band potential is merely slightly more positive than the H_2O oxidation potential, ii) it suffers from imbalanced electron and hole mobility, and iii) its surface inertness hinders the absorption and activation of CO_2 and H_2O molecules. Among the various approaches developed to address these shortcomings, constructing heterojunctions or heterophase junctions by combining SiC with another semiconductor or an allotrope of SiC has been proven to be the most effective method for enhancing photocatalytic activity.[21–22] In this study, the powder-type and single-crystal-type SiC@WO_3 heterojunctions and their heat-treated derivatives were designed and utilized as model systems to investigate the impact of BIEF on photocatalytic activity. The selection of WO_3 as a partner for constructing heterojunctions with SiC is based on the following considerations: i) WO_3 and SiC can form a Z-scheme heterojunction with a wide effective band gap that meets the thermodynamic requirements for CO_2 reduction with H_2O. ii) Unlike previously reported semiconductors combined with SiC,[23,24] WO_3 nanoplates can be facilely coupled with SiC nanoparticles to form well-defined contact interfaces through the solvothermal method.[25] In addition, WO_3 film can be easily sputtered onto semiconductor substrates to fabricate single-crystal heterojunctions with fine-controlled interfaces,[26] enabling direct comparison between powder and single-crystal systems to derive robust conclusion. iii) WO_3 surface can be readily modified by reduction treatments to generate non-stoichiometric WO_{3-x} and metallic W, providing a feasible route to tune the interfacial composition, heterojunction structure, and BIEF intensity.

Through our investigation of the SiC@WO_3 heterojunction, we reveal a clear linear dependence of the BIEF intensity and the total number of effective photoelectrons involved in the photocatalytic reduction of CO_2 with H_2O to yield CH_4 /CO and O_2 under visible illumination. A stronger BIEF significantly promotes the separation and transfer of photogenerated charges from WO_3 to SiC, thereby enhancing the photocatalytic activity. The SiC@WO_2 /WO_3 sample, exhibiting the largest BIEF intensity, achieved the greatest photocatalytic activity. This work reveals, for the first time, a quantitative correlation between BIEF intensity and photocatalytic activity, which is of great significance for refining and expanding the heterojunction photocatalysis theory, as well as for designing highly efficient composite photocatalysts.

2. Results and Discussion

2.1. Heterostructure Feature and Modulation of Samples

The powder SiC@WO_3 sample, designated as SW25, was synthesized by thermal hydrolysis of tungsten precursors on SiC nanoparticles. Subsequently, a series of reduced samples, denoted as SW-T, was prepared by treating SW25 in a hydrogen atmosphere at different temperatures (T °C). X-ray diffraction (XRD) patterns (**Figure** 1a and zoom regions) confirm that the WO_3 component in SW25 keeps its monoclinic phase (marked with ▲), while SiC remains in the cubic phase (marked with ★). Scanning electron microscopy (SEM) and transmission electron microscopy (TEM) images suggest that SiC nanoparticles are firmly adhered to WO_3 nanoplates in the SW25 composite (Figure 1b; Figure S1a–c, Supporting Information). Further TEM and High-resolution TEM (HRTEM) images support this microstructure, showing intimate contact between SiC nanoparticles (red dotted line) and WO_3 nanoplates (blue dotted line) (Figure 1c; Figure S1d–g, Supporting Information). Clear lattice fringes with inter-planar spacing of 0.217 and 0.262 nm, corresponding respectively to the (200)[27] and (202)[28] facets of SiC and WO_3, and seamless transitional interface unambiguously indicate the formation of a well-defined heterojunction between SiC and WO_3 (Figure 1d). Additional evidence for the close interfacial contact is supported by High-Angle Annular Dark-field scanning transmission electron microscope (HAADF-STEM) images and mapping images of C, Si, W, and O elements (Figure S2, Supporting Information). Collectively, these results indicate that a heterojunction forms at the interface between SiC and WO_3 for SW25.

X-ray photoelectron spectroscopy characterization (XPS) also provides the formation of a heterojunction between SiC and WO_3. As shown in Figure 1e, the bare SiC exhibits two C 1s peaks at 283.0 eV (C1, Si—C bond) and 284.8 eV (C2, adventitious carbon), respectively. In the SW25 sample, three C peaks are observed at 283.2 (C1), 284.7 (C3), and 284.8 eV (C2). The C1 peak, attributed to bulk Si—C, shows a positive shift of 0.2 eV, while the new C3 peak, situated between C1 and C2, is assigned to carbon species formed at the interface between SiC and WO_3.[27] The Si 2p spectrum of bare SiC (Figure 1f) shows a symmetric peak at 101.0 eV, consistent with pure SiC.[23] In contrast, the SW25 sample exhibits two peaks at 101.2 eV (Si1, bulk SiC) and 103.3 eV (Si2), the latter indicating a new silicon environment arising from interfacial interaction. For O1s (Figure 1g), pristine WO_3 displays peaks at 530.42 eV (O1, lattice oxygen) and 532.06 eV (O2, surface oxygen species),[29] respectively. The SW25 sample shows an additional peak at 533.02 eV (O3), assigned to interface oxygen. The W 4f peaks of nude WO_3 (Figure 1h) show spin-orbit doublets corresponding to W^{6+} and a minor W^{5+} contribution.[30] In the SW25 sample, these peaks shift toward lower binding energy. The collective changes, including increased binding energy for C and Si, decreased binding energy for W and O, and the emergence of new interfacial species (C3, Si2, and O3), provide strong evidence for a strong electronic interaction between SiC and WO_3, confirming the successful formation of a heterojunction.

Additionally, the Raman bands of W-O vibrations in the SW25 sample shift to lower wavenumbers compared to those of pure WO_3 (Figure 1i; Figure S3, Supporting Information). For the SW-T samples, the Raman bands at 265 cm^{-1} (O-W bending modes) and 714 cm^{-1} (O-W stretching modes) undergo a further blueshift relative to SW25 (Figure 1i).[31] Among all reduced samples, SW-600 shows the most pronounced shift toward lower wavenumber. These results suggest that the reduction treatment can effectively modify the interfacial properties of the SiC@WO_3 heterojunction, including the BIEF intensity of the heterojunction and its photocatalytic performance. The reasons for this will be discussed later.

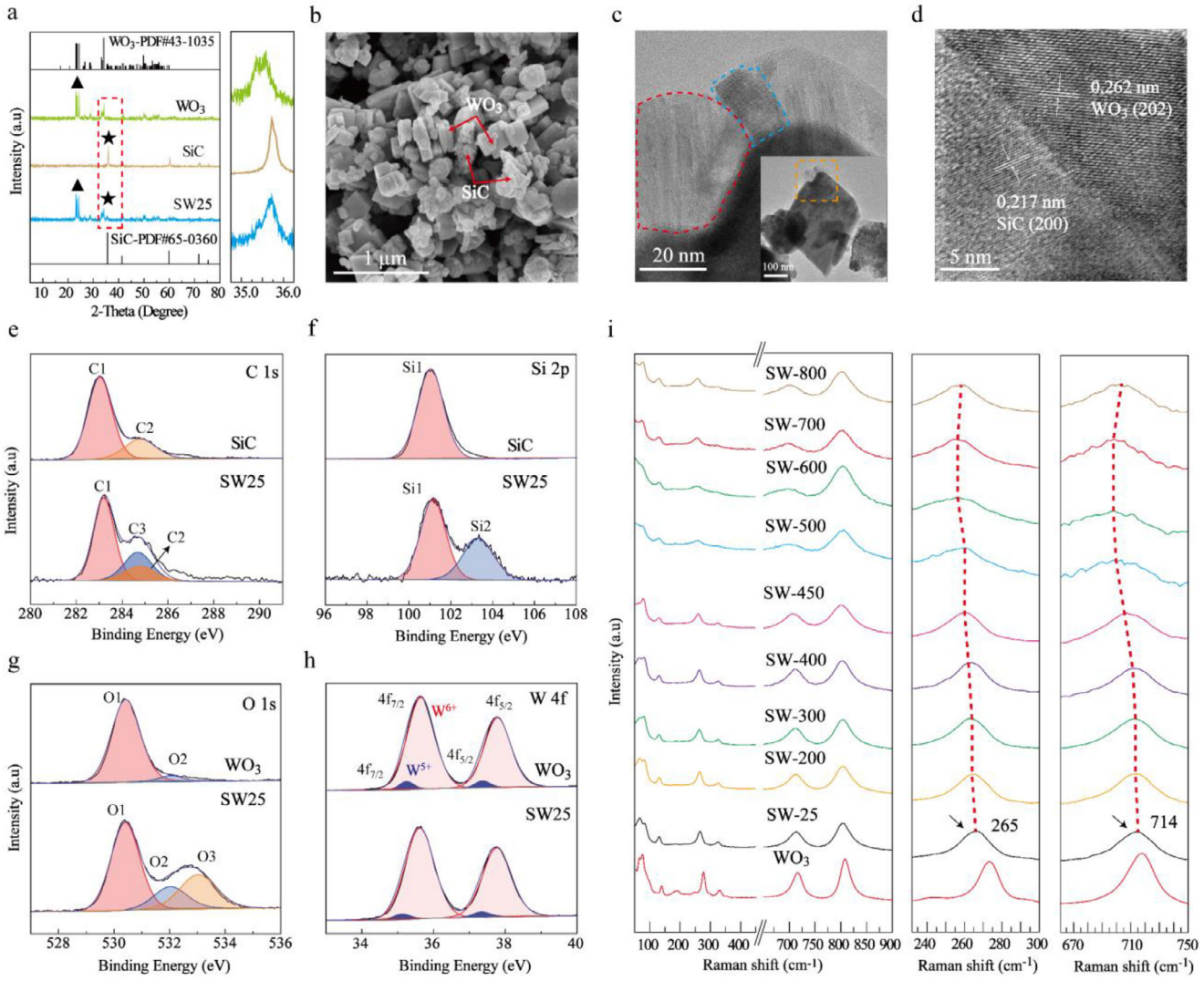

Figure 1. a) XRD patterns of WO_3, SiC, and SW25. b) SEM image of SW25. c,d) TEM and the corresponding HRTEM images of SW25. e–h) XPS spectra of C 1s, Si 2p, O 1s, and W 4f for pure SiC, pure WO_3, and SW25. i) Raman spectra of WO_3 and their changes in SW-T samples with reduction temperature (T) and the corresponding zoom regions.

2.2. Photocatalytic Activity of Samples

The photocatalytic behavior of SW25 and SW-T samples was evaluated by the reaction of CO_2 with H_2O under visible light illumination, as shown in **Figure 2**. CH_4 and CO are identified as the two main reduction products for all samples. Except for bare SiC, all SW-T samples produce higher yields of CH_4 than CO (Figure 2a). Multiple factors, including the reaction conditions and photocatalyst structure, actually control product selectivity in photocatalytic CO_2 reduction with H_2O.[32,33] The high CH_4 selectivity and consistently low CO yields observed over the SW-T samples may be attributed to alterations in surface active sites following reduction treatment, especially the formation of the interfacial species between SiC and WO_3. A detailed molecular mechanistic explanation of this selectivity will require further in-depth investigation, though the general conclusion of this study remains unaffected. Notably, all SW-T samples exhibit substantially higher total yields (CO + CH_4) than bare SiC. Moreover, the CH_4 evolution profile follows a volcanic trend with increasing reduction temperature. The maximum CH_4 evolution occurs over SW-600, which is *ca.* 5 times higher than its CO evolution amount, 7 times higher than the CH_4 yield of SiC, and 3 times higher than the CH_4 yield of SW25. However, a sharp decrease in CH_4 production is observed when the reduction temperature is raised from 700 to 800 °C (Figure 2a). Furthermore, the sum of CH_4 and CO yield on SW-600 significantly exceeds that of a mechanical mixture of SiC-600 and WO_3-600 (Figure 2b). Impressively, the CH_4 yield on SW-600 is even higher than the combined CH_4 yield on the three samples (SiC-600, WO_3, and WO_3-600).

Since the generation of one CH_4 molecule needs eight electrons ($CO_2 + 8H^+ + 8e^- \rightarrow CH_4 + 2H_2O$), and the production of one CO molecule consumes two electrons ($CO_2 + 2H^+ + 2e^- \rightarrow CO + H_2O$),[34] we introduce the concept of the number of effective photoelectron (N_{EPN}) to more accurately represent the

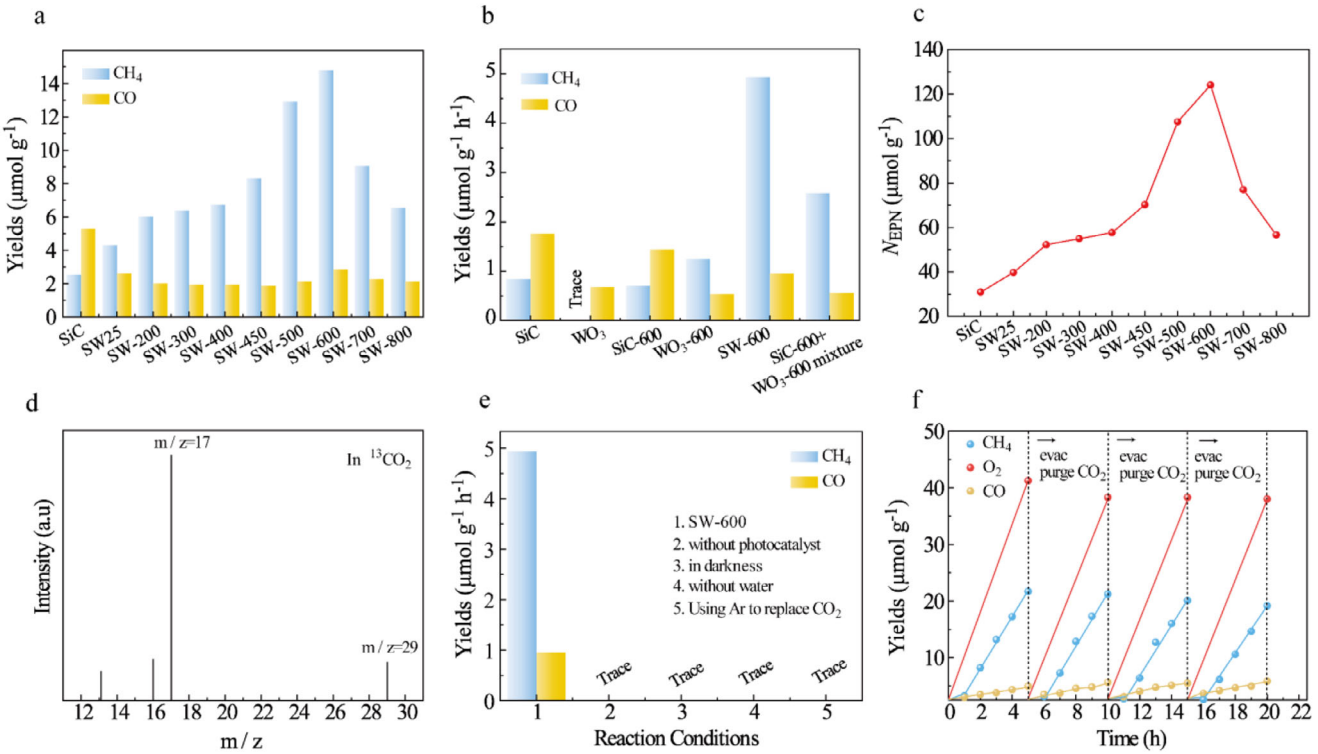

Figure 2. Photocatalytic behavior of samples SiC, SW25, and SW-T under visible light. a) Effect of the treatment temperature on the CH_4 and CO yields. b) Photocatalytic CO_2 reduction rate on SW-600 and reference samples. c) Change in the effective photoelectron number (N_{EPN}) with the treatment temperature. d) GC-MS spectra of the photocatalytic product with $^{13}CO_2$ instead of CO_2 as a reactant for SW-600. e) Reduction products of CO_2 in different reaction conditions. f) Photocatalytic activity stability test of SW-600.

photocatalytic activity of samples and facilitate the investigation of structure-activity relationships. N_{EPN} is defined as the total number of electrons required to generate CO and CH_4 according to the following Equation (1).

$$N_{EPN} = 2N(CO) + 8N(CH_4) \quad (1)$$

As shown in Figure 2c, the N_{EPN} value varies with the reduction temperature from room temperature to 800 °C. The change in N_{EPN} could be divided into three stages: a slow increase from 200 to 400 °C, a rapid rise between 400 and 600 °C, and a sharp decline above 600 °C. The maximum N_{EPN} value of 123 μmol g^{-1} is achieved with SW-600, which is *ca.* 5 times bigger than that of SW25.

The results suggest that the reduction treatment may modify the composite structure and, consequently, alter the photocatalytic activity, with 600 °C being the optimal reduction treatment temperature for maximizing CH_4 yield. Although the reduction treatment affects the morphology and BET surface area of the SW-T samples, these properties do not directly correlate with the enhanced photocatalytic performance (Figures S4 and S5 and Table S1, Supporting Information). The linear increase in CH_4 evolution with light intensity confirms that the reaction is light-driven (Figure S6, Supporting Information).[27] Isotopic labelling experiments using $^{13}CO_2$ showed that the products were $^{13}CH_4$ (m/z = 17) and ^{13}CO (m/z = 29) over SW-600, indicating that the carbon source originated from the supplied CO_2 rather than the photocatalyst itself (Figure 2d). No products are detected when Ar (argon) is used instead of CO_2, or in the absence of H_2O, light, or photocatalyst (Figure 2e), further verifying the photocatalytic nature of the reaction. Cyclic tests demonstrate that SW-600 exhibits stable performance over five consecutive cycles (20 h in total), with an average CH_4 yield of 21.7 μmol g^{-1} and nearly stoichiometric O_2 evolution (41.3 μmol g^{-1}) (Figure 2f). Based on the yields of CH_4 (22 μmol g^{-1}), CO (4 μmol g^{-1}), and O_2 (42 μmol g^{-1}) over a 5 h reaction, the N_{EPN} is calculated as *ca.*184 μmol g^{-1}, while the number of holes consumed is estimated as *ca.* 168 μmol g^{-1} based on the oxidation reaction ($2H_2O + 4h^+ \rightarrow O_2 + 4H^+$). This minor discrepancy may be attributed to experimental error and surface oxidation of the photocatalyst, but overall, the charge transfer remains essentially balanced. Furthermore, XRD patterns of SW-600 exhibit only minor changes before and after the photocatalytic reaction (Figure S7, Supporting Information), suggesting good structure stability under photocatalytic conditions

2.3. Band Alignment and BIEF Intensity (E_{bi}) Determination of the Heterojunction

Electron structure parameters of SiC and WO_3 were characterized by ultraviolet photoelectron spectroscopy (UPS) and UV–vis diffuse reflectance spectroscopy. The valence band levels (E_{VB}) of SiC and WO_3 relative to vacuum energy levels are determined to

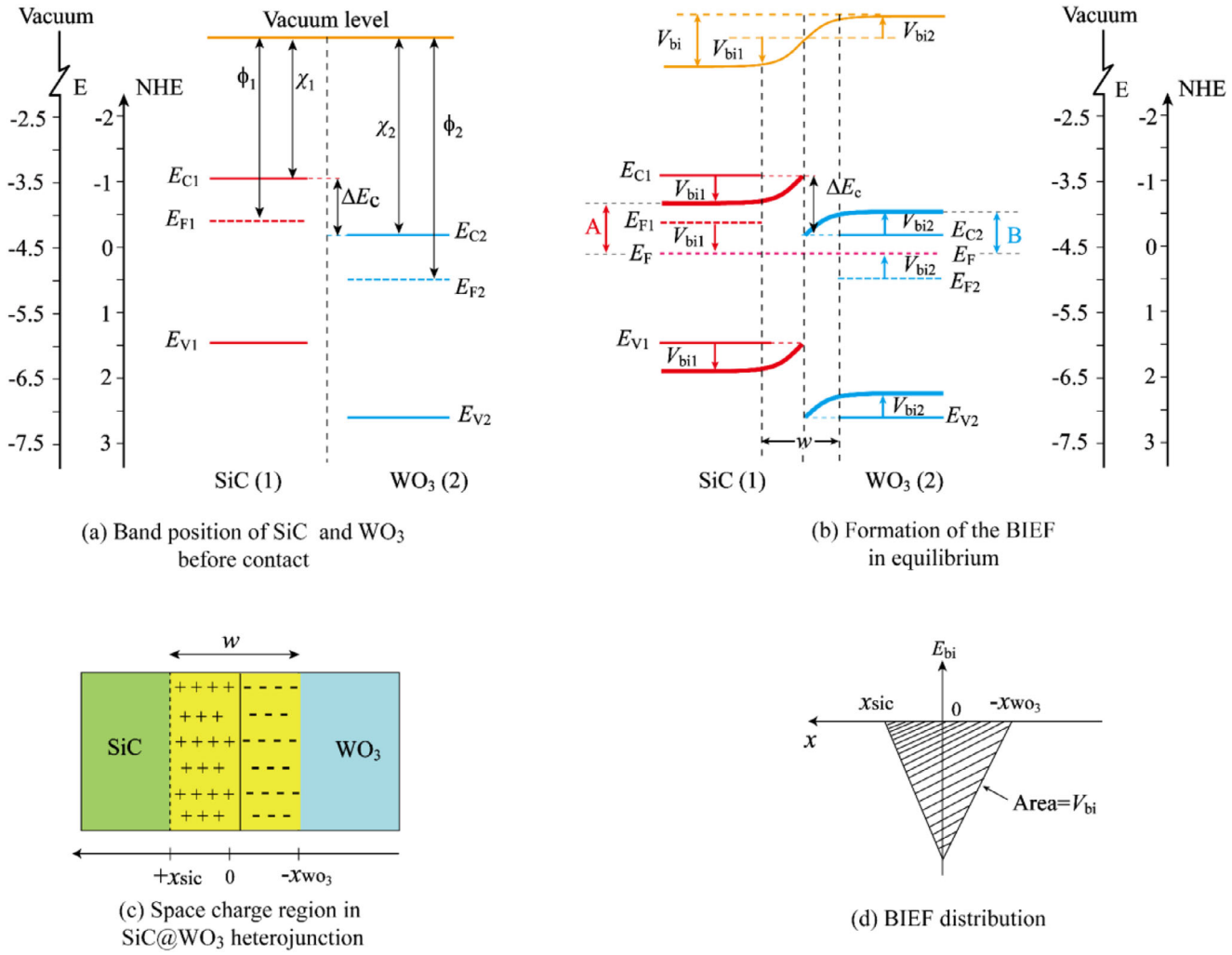

Figure 3. a) Electronic structure diagrams of SiC and WO_3 before contact. b) Electronic structure diagram of the idealized SiC@WO_3 heterojunction. c) Space charge region diagrams of the SiC@WO_3 heterojunction. d) BIEF distribution within the SiC@WO_3 heterojunction interface.

be −5.91 and −6.81 eV (Figure S8a,b, Supporting Information), respectively, as calculated by Equation (2),

$$E_{VB} = h\nu + E_{Fermi} - E_{Cutoff} \quad (2)$$

where $h\nu$ denotes the He I excitation energy of 21.22 eV.[35] The band gap energies (E_g) of SiC and WO_3 are found to be 2.48 and 2.78 eV, respectively, with respect to the vacuum level (Figure S8c,d, Supporting Information). Accordingly, the conduction band levels (E_{CB}) of SiC and WO_3 are calculated to be −3.43 and −4.03 eV (vs vacuum), respectively. Based on the relationship between the vacuum energy level (E_{vacuum}) and the RHE potential (E_{RHE}), the E_{CB} and E_{VB} versus RHE are converted to −1.01 and 1.47 V for SiC and −0.41 and 2.37 V for WO_3 (Table S2, Supporting Information), respectively. Therefore, the valence and conduction bands of SiC and WO_3 form a staggered alignment configuration (Figure S9, Supporting Information). A schematic of the energy band structures before contact is shown in **Figure 3a**. Since the bigger work function of WO_3 (5.05 eV)[36] than SiC (4.0 eV)[37] (Table S2, Supporting Information), i.e., a higher Fermi energy level (E_F) of SiC than WO_3, free electrons would transfer spontaneously from SiC to WO_3 upon intimate contact until their Fermi levels align to form a heterojunction.[9,29,38] This leads to the establishment of a BIEF directed from SiC (marked as 1) to WO_3 (marked as 2) at the heterojunction interface. Consequently, the energy bands (both VB and CB) of SiC bend upward due to the downward shift of its E_F, while those of WO_3 would bend downward owing to the upward shift of its E_F. A detailed illustration of the heterojunction formation process is provided in Figure S10 (Supporting Information), and the resulting electronic structure relationship is depicted in Figure 3b.[39]

In physics, the built-in electric field intensity (E_{bi}) of a heterojunction is defined as the built-in potential per unit distance in Equation (3),

$$E_{bi} = \frac{V_{bi}}{w} \quad (3)$$

where V_{bi} represents the built-in electric potential, w is the breadth of the depletion layer of the heterojunction.[40]

Assuming that w is a constant, E_{bi} is proportional to V_{bi}. The impact of E_{bi} on photocatalytic activity, in other words, is comparable to that of V_{bi}. To the best of our knowledge, there are currently three methods to acquire V_{bi} or E_{bi} for a heterojunction material in the literature.

(1) Based on the band alignment shown in Figure 3a,b, V_{bi} is equal to the difference between the Fermi energy levels of the two semiconductor components in Equation (4),[41,42]

$$V_{bi} = \left(\frac{E_{F1} - E_{F2}}{q}\right) \tag{4}$$

where E_{F1} and E_{F2} are respectively the Fermi energy levels of SiC and WO_3, and q is the elementary charge. The difference in Fermi energy levels between the two components can be determined by separately measuring the surface work function value of the two components using the Scanning Kelvin Probe method (SKP) under dark conditions. The work function (ϕ) and the Fermi energy level (E_F) of a semiconductor conform to the following Equation (5),[43]

$$E_F = E_{vac} - \phi \tag{5}$$

where E_{vac} is the vacuum energy level. According to the SKP principle, the work function of the sample (ϕ_{sample}), the work function of the tip (ϕ_{tip}, e.g., ϕ_{Au} = 5.1 eV), and the contact potential difference (CPD) adhere to the following mathematical Equation (6),[27]

$$\phi_{sample} = \phi_{tip} + q \times CPD \tag{6}$$

For the composite semiconductors consisting of SiC and WO_3, the V_{bi} can be estimated by separately measuring their CPD value through Equation (7),

$$\begin{aligned} V_{bi} &= \frac{(E_{vac}-\phi_1)-(E_{vac}-\phi_2)}{q} \\ &= \frac{\phi_2-\phi_1}{q} \\ &= CPD_2 - CPD_1 \end{aligned} \tag{7}$$

(2) According to the band alignment illustrated in Figure 3a,b and previous literatures,[11,44,45] V_{bi} value can also be expressed in Equation (8) as the sum of the band bending value on the SiC side (V_{bi1}) and the band bending value on the WO_3 side (V_{bi2}), and E_F here specifically denotes the Fermi energy level of SiC@WO_3 composite in equilibrium conditions,

$$V_{bi} \equiv \left(\frac{E_{F1} - E_{F2}}{q}\right) = V_{bi1} + V_{bi2} \tag{8}$$

Given Equation (9):

$$\begin{aligned} A &= k_B\ T\ \ln\frac{N_{c1}}{N_{d1}} = \left(E_{c1} - E_F\right) - qV_{bi1} \\ B &= k_B\ T\ \ln\frac{N_{c2}}{N_{d2}} = \left(E_{c2} - E_F\right) + qV_{bi2} \end{aligned} \tag{9}$$

We derive Equation (10),

$$\begin{aligned} V_{bi1} &= \frac{(E_{c1}-E_F)}{q} - \frac{k_B T}{q}\ln\frac{N_{c1}}{N_{d1}} \\ V_{bi2} &= \frac{(E_F-E_{c2})}{q} + \frac{k_B T}{q}\ln\frac{N_{c2}}{N_{d2}} \end{aligned} \tag{10}$$

Substituting Equation (10) into Equation (8) yields Equation (11),

$$\begin{aligned} V_{bi} &= \left[\frac{(E_{c1}-E_F)}{q} - \frac{k_B T}{q}\ln\frac{N_{c1}}{N_{d1}}\right] + \left[\frac{(E_F-E_{c2})}{q} + \frac{k_B T}{q}\ln\frac{N_{c2}}{N_{d2}}\right] \\ &= \frac{\Delta E_c}{q} + \frac{k_B T}{q}\ln\frac{N_{d1}\times N_{c2}}{N_{d2}\times N_{c1}} \end{aligned} \tag{11}$$

where k_B is the Boltzmann constant, T is the thermodynamic temperature, $\Delta E_c = E_{c1} - E_{c2}$ represents the conduction band offset between SiC and WO_3 (equivalent to the difference in their electron affinities, χ). N_{c1} and N_{c2} denote the effective density of state in the CB of SiC and WO_3 (constant for a given semiconductor and temperature). N_{d1} and N_{d2} represent the net donor concentrations in SiC and WO_3 regions of the SiC@WO_3 composites, respectively.[46] N_d of a bulk semiconductor can be measured through the Hall effect, though accurate determination remains challenging for powdered heterostructure photocatalysts.[47]

(3) The third method involves analyzing the variation of space charge density with distance x across the space charge region (width w) within the framework of an abrupt junction model (Figure 3c). According to Gauss's law, the built-in electric field strength in a 1D model can be described by Equation (12),[41]

$$dE_{bi}(x)/dx = Q(x)/\epsilon \tag{12}$$

Thus, we obtain Equation (13),

$$\begin{aligned} \frac{dE_{bi}(x)}{dx} &= -\frac{qN_{d2}}{\epsilon_2},\ -x_2 < x < 0 \\ \frac{dE_{bi}(x)}{dx} &= \frac{qN_{d1}}{\epsilon_1},\ 0 < x < x_1 \end{aligned} \tag{13}$$

By integrating Equation (13) under the boundary condition that E_{bi} intensity is zero at the boundaries $x = -x_2$ and $x = x_1$, we obtain Equation (14),

$$\begin{aligned} E_{bi}(x) &= -\frac{qN_{d2}}{\epsilon_2}\left(x + x_2\right),\ -x_2 < x < 0 \\ E_{bi}(x) &= \frac{qN_{d1}}{\epsilon_1}\left(x - x_1\right),\ 0 < x < x_1 \end{aligned} \tag{14}$$

Here, x is the coordinate in the space charge region, $Q(x)$ is the total charge concentration, ϵ is the product of the relative dielectric constant and the free space permittivity, N_{d1} and N_{d2} represent the total donor concentration in the SiC and WO_3 regions, respectively. As illustrated in Figure 3d, the E_{bi} intensity enlarges from $-x_2$ to x_1 before reaching a maximum value at the coordinate $x = 0$, and the shaded triangle area represents the built-in electric potential value.

Because E_{bi} and V_{bi} adhere to Equation (15),

$$E_{bi}(x) = -dV_{bi}(x)/dx \tag{15}$$

Then we can obtain Equation (16),

$$\begin{aligned} V_{bi}(x) &= \frac{qN_{d2}}{\epsilon_2}\left(\frac{x^2}{2} + x_2 x\right),\ -x_2 < x < 0 \\ V_{bi}(x) &= -\frac{qN_{d1}}{\epsilon_1}\left(\frac{x^2}{2} - x_1 x\right),\ 0 < x < x_1 \end{aligned} \tag{16}$$

Equation (16) shows that V_{bi} at the junction interface depends on the donor concentration and dielectric constants, and can be approximated as a quadratic function of the coordinate (x) on

each side of the junction. However, it is impractical to determine V_{bi} at every point by directly measuring the local donor concentration. Instead, Kelvin Probe Force Microscopy (KPFM), which offers nanoscale spatial resolution and millivolt-level sensitivity, can be employed to map the surface potential and thereby characterize the distribution of V_{bi}. In this study, a well-defined SiC@WO_3 heterojunction was fabricated by sputtering a WO_3 film onto a single-crystal SiC substrate. The junction interface ($x = 0$) was identified using height and phase images. The V_{bi} profile across the space charge region (from $-x_2$ to x_1) was measured via KPFM and fitted to a quadratic function according to Equation (16). The E_{bi} distribution was then obtained by differentiating the V_{bi} profile using Equation (14), yielding the maximum E_{bi} intensity (Figure 3d). This approach has been employed in the study of BIEF in the TiO_2 heterophase junction, carbon nitride homojunction, and the inter-facet potential distribution on Cu_2O particles by Li, et al.[48–50]

In addition to the three methods above, some researchers have suggested that the BIEF intensity of a material can be calculated using Kanata's model, as presented in Equation (17), and Couy-Chapman's model, as outlined in Equation (18).[51,52]

$$E = \left(\frac{-2V_s\rho}{\varepsilon\varepsilon_0}\right)^{1/2} \tag{17}$$

$$\rho = \left(8cN\varepsilon_0\varepsilon_r k_B T\right)^{1/2} \sin h\left(\frac{e\zeta}{2k_B T}\right) \tag{18}$$

In fact, Kanata's model is unsuitable for quantifying the BIEF in a heterojunction. First, Kanata's model relies solely on parameters from a single semiconductor (e.g., surface voltage V_s, surface charge density ρ, the vacuum dielectric constant $\epsilon_0 = 8.85 \times 10^{-12}$ F m^{-1}) and low-frequency dielectric constant ϵ). However, the BIEF in a heterojunction originates from the interface region between two distinct semiconductors, meaning its intensity should inherently depend on the properties of the two semiconductors. Consequently, the obtained electric field from this model reflects only the surface properties of an individual component rather than the true BIEF of the heterojunction.[51] Second, the electric field calculated by Kanata's model is generally referred to as the internal electric field (IEF).[53] instead of the built-in electric field (BIEF).[12,15] This model was initially developed to calculate the IEF within a single bulk semiconductor, such as bismuth oxyiodide with different reduction degrees of I (BiOI, $Bi_4O_5I_2$, Bi_5O_7I),[54] carbon nitride or perylene imide supramolecular photocatalyst with varying levels of crystallization,[55,56] and so on. Although the model has been adopted to rationalize the role of the electric field in heterojunctions (such as ZnTCPP/THPP,[57] CoP/BVO,[58] and TiO_2/CeO_2[59]), its application in these contexts is generally limited to qualitative comparisons (e.g., considering only ϵ of one semiconductor or lacking a precise numerical value). Therefore, Kanata's model is not applicable for quantitatively determining the exact value of BIEF in this study.[13,53]

According to the analysis above, method (1) (based on surface work function difference) and method (3) (based on surface potential distribution) are both relatively straightforward and suitable for measuring V_{bi} or E_{bi} of the heterojunction of powder or single-crystal photocatalyst. Therefore, in this work, the two methods were selected to obtain V_{bi} or E_{bi} of the powder SW-T and single-crystal sc-SW-T samples.

2.3.1. Quantitative Relationship Between E_{bi} Intensity and N_{EPN} for the Powder Samples

Following method (1), the surface work function of the pure SiC-T and the pure WO_3-T was determined separately (Figure S11, Supporting Information), and the built-in potential (V_{bi}) value of the SiC@WO_3 heterojunction samples was calculated using Equation (7). The V_{bi} value of SW25 is determined to be 0.17 V. For the SW-T samples, the V_{bi} value gradually increases from 0.2 to 0.5 V as the reduction temperature rises from 200 to 600 °C (**Figure 4a**). With the reduction temperature increasing further to 700 and 800 °C, the V_{bi} value declines to 0.33 and 0.26 V, respectively (Figure 4a). Obviously, the change in V_{bi} follows a volcanic curve with increasing reduction temperature, and the maximum value is observed for SW-600. A linear correlation is revealed between the V_{bi} value and the N_{EPN} of SW-T samples (Figure 4b). As mentioned above, since the influence of E_{bi} on the photocatalytic activity is equivalent to that of V_{bi} under a constant depletion width, the above results demonstrate that a stronger E_{bi} (or V_{bi}) at the SiC@WO_3 interface leads to higher photocatalytic activity in the photocatalytic reaction of CO_2 with H_2O to CH_4 /CO and O_2. According to the slope of the fitted line, the N_{EPN} increases by 0.25 μmol g^{-1} for every 1 kV increase in V_{bi} for the powder sample.

2.3.2. Quantitative Relationship Between E_{bi} Intensity and N_{EPN} for the Single Crystal Samples

Using method (1) to determine the E_{bi} of powder heterojunction, by separately measuring the work function of the two bare semiconductor components, is an indirect method, and may yield results that deviate from the actual BIEF of heterojunction in theory. To further verify the quantitative relationship between the E_{bi} intensity and N_{EPN} for a heterojunction photocatalyst, single-crystal heterojunction samples (sc-SW25) with well-defined heterojunction interfaces were fabricated for direct E_{bi} measurement using method (3). The sc-SW25 samples were prepared by sputtering a WO_3 film on a SiC single crystal substrate (Figure S12, Supporting Information). XRD characterizations (Figure S13, Supporting Information) show that the phase compositions of sc-SiC and sc-SW25 samples are consistent with those of the corresponding powder samples. Reduction-treated single-crystal samples (sc-SW-T) were then obtained using the same reduction process at varying temperatures as applied to the powder SW-T samples.

Precise localization of the interface between SiC and WO_3 is crucial for measuring the E_{bi} intensity of sc-SW-T samples with an exposed, clean cross-section (Figure S14, Supporting Information). Topography images of all sc-SW-T samples (Figure S15a_1–i_1, Supporting Information) show a height difference of ≈1 μm between SiC and WO_3, consistent with the thickness of the sputtered WO_3 film. Simultaneously, the corresponding phase images (Figure S15a_2–i_2, Supporting Information) exhibit a distinct contrast across the boundary, reflecting differences in

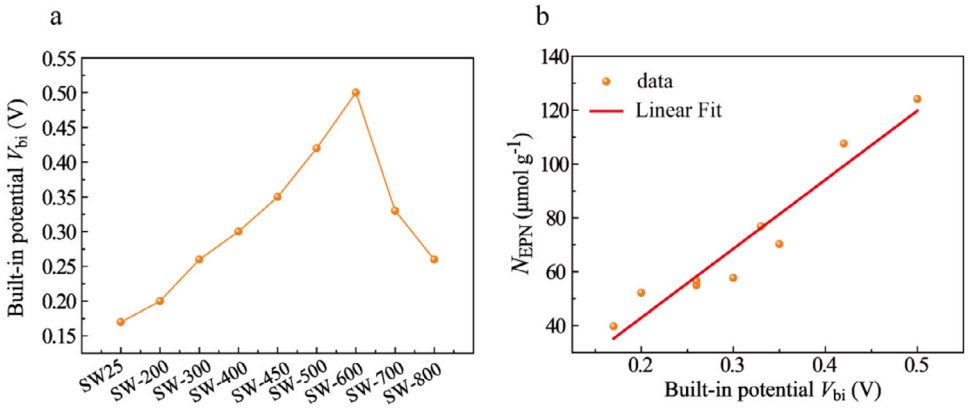

Figure 4. Correlation between photocatalytic activity and built-in electric potential V_{bi} for the powder SW-T samples. a) Change in V_{bi} with the reduction temperature, and b) Change in the effective photoelectron number N_{EPN} with V_{bi}.

hardness or composition between the two phases (attributable to the commercial SiC substrate and the magnetron-sputtered WO_3 film). Collectively, the topography and phase features enable precise localization of the interface. Based on this localization, the E_{bi} intensities of sc-SW25 and sc-SW-600 samples are first calculated and compared. In detail, the V_{bi} distribution across the interfacial junction is recorded and fitted by Equation (16). Differentiating the fitting curve according to Equation (14) yields an E_{bi} intensity of *ca.* 6.8 kV cm^{-1} for sc-SW25 (**Figure** 5a,b), which exceeds previously reported BIEF value for TiO_2 heterophase junctions and carbon nitride homojunction.[48,50] In comparison, the maximum E_{bi} intensity of sc-SW-600 reaches *ca.* 18.1 kV cm^{-1}. To confirm the enhancement effect of interface treatment on E_{bi} intensity, sc-SW-T series samples were characterized (Figure S15, Supporting Information). The results reveal that the E_{bi} intensities follow a volcanic-shaped curve with increased reduction temperature. It initially increases slowly and then rises rapidly to a peak value of ≈18.1 kV cm^{-1}. Then, the E_{bi} intensity sharply declines as the

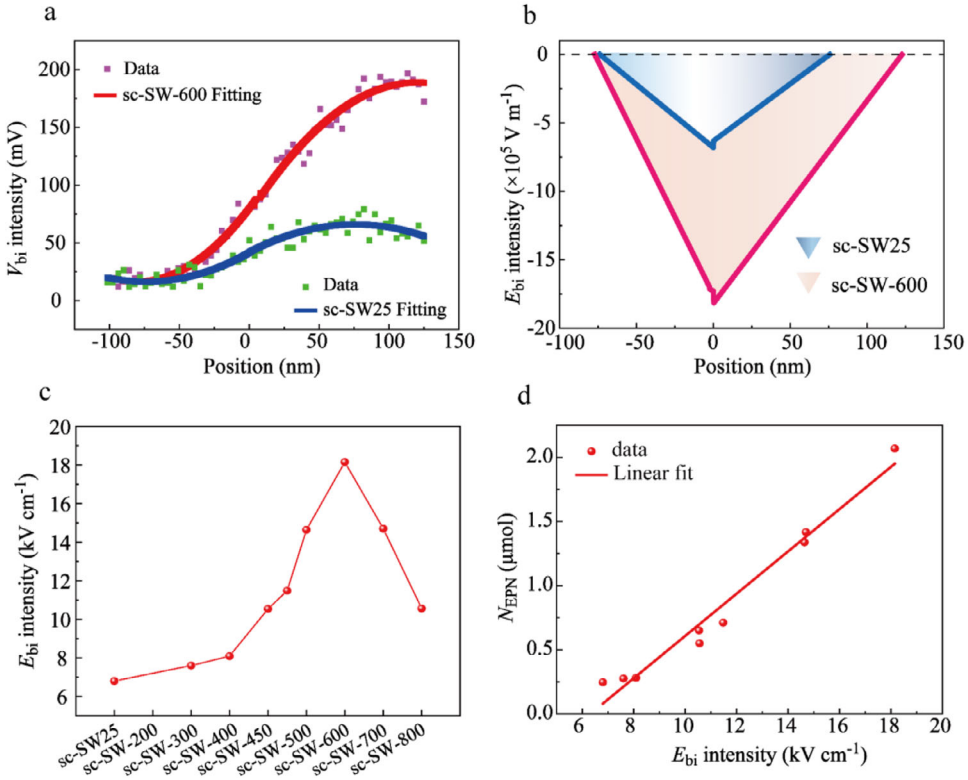

Figure 5. Correlation between photocatalytic activity and built-in electric field E_{bi} for the single crystal sc-SW-T samples. a) Distribution and fitting of V_{bi}. b) E_{bi} intensity changes with distance across the heterojunction interface. c) Change in E_{bi} with the reduction temperature. d) Change in N_{EPN} with E_{bi}.

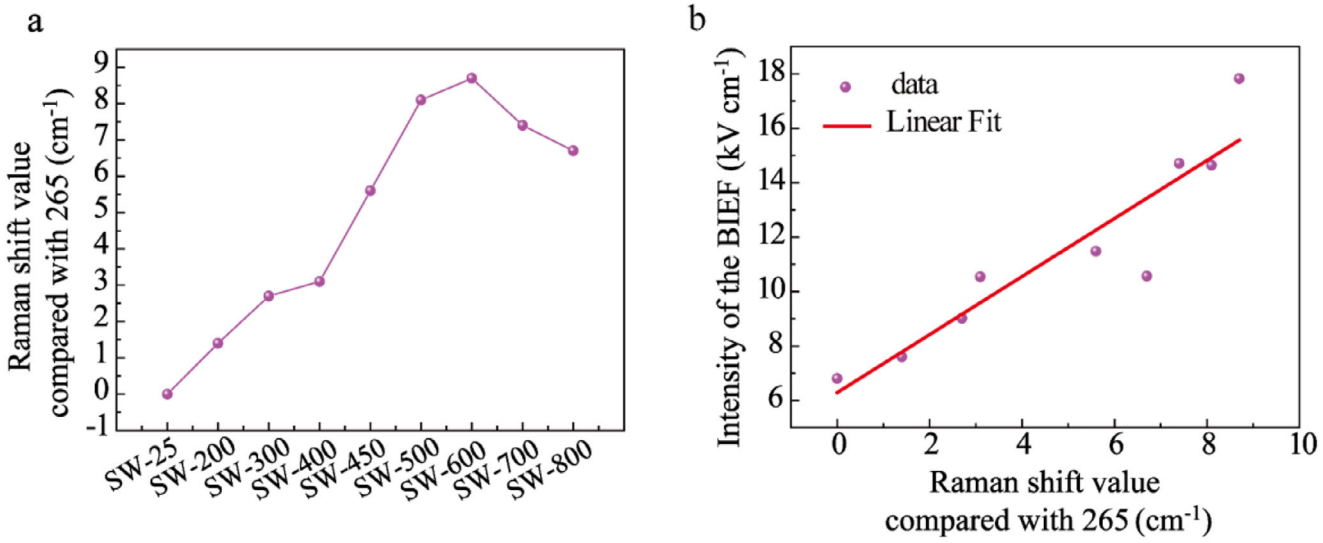

Figure 6. Correlation between Raman shift and BIEF for SW-T samples. a) Change in the Raman shift value near 265 cm^{-1}. b) Change in BIEF value with the Raman shift value.

reduction temperature increases from 700 to 800 °C (Figure 5c). The trend confirms that thermal treatment effectively modulates the E_{bi} in the heterojunction.

The photocatalytic activity of the as-fabricated sc-SW-T samples was also evaluated (Figure S16, Supporting Information). The single-crystal samples exhibit a trend in total activity similar to that of the powder samples, with the highest activity observed for the sc-SW-600 sample. However, the absolute activity is significantly lower than that of the SW-600 sample. A notable difference is that CO is the dominant product below 450 °C for the single-crystal sample, which may result from the different relative proportions of SiC and WO_3 between the two counterparts. Accordingly, we have reason to believe that the single-crystal sample exhibits the same heterojunction feature as the powder samples. Figure 5d shows that the N_{EPN} value of sc-SW-T samples displays a clear linear dependence on E_{bi} intensity. The fitted line has a slope of 0.16, indicating that N_{EPN} increases by 0.16 μmol for every 1 kV cm^{-1} increase in E_{bi}. These findings unequivocally demonstrate that the photocatalytic activity of the composite heterojunction depends on the intensity of the built-in electric field, and the stronger the built-in electric field, the higher the photocatalytic activity.

3. Discussion

3.1. Reason for the E_{bi} Intensity Change with Reduction Treating Temperature

Since the BIEF is generated at the heterojunction interface between two coupled semiconductors, the interfacial structure and composition play a critical role in determining E_{bi} intensity. In WO_3, the Raman band at 274 cm^{-1} is attributed to the O-W bending vibration mode. For the SW25 sample, this band shifts negatively to 265 cm^{-1} (Figure S3, Supporting Information), indicating enhanced interaction between SiC and WO_3. It is suggested that Si—O—W bonds form at the interface, with Si contributed from the SiC side and W from the WO_{3-x} side. This observation aligns with the presence of new interfacial species conjectured from the XPS spectra (Figure 1e–h). The change of the Raman shift at ≈265 cm^{-1} with reduction temperature is presented in **Figure 6a**. Obviously, the Raman shift value increases progressively from 25 to 600 °C, peaking at 600 °C, and then decreases from 700 to 800 °C. Interestingly, Raman shift exhibits a linear relationship with increasing BIEF strength (Figure 6b), a trend that closely mirrors the linear correlation observed between photocatalytic activity and BIEF intensity. This parallel strongly suggests that the Raman shift value serves as a potential descriptor for estimating BIEF intensity. The generation of such an interfacial species–particularly Si—O—W bonds–enables intimate contact between SiC and WO_3, thereby forming a high-quality heterojunction. These covalent bonds can act as specific bridging sites, enhancing interface adhesion and reducing electron transfer resistance, thereby effectively mitigating the poor contact and high charge recombination often encountered in conventional heterojunction systems.[60]

Changes in the crystal phase, element states, and morphology of the SW-T samples with increasing reduction temperature were characterized by XRD, XPS, and TEM. The XRD patterns show that the diffraction signals of WO_3 are stronger than those of SiC (Figure S17a, Supporting Information). As for SW-T samples, their XRD patterns can be divided into three stages. In the first stage (200–450 °C), the SW-T samples generally remain predominantly WO_3. In the second stage (450–600 °C), the intensity of WO_3 diffraction peaks decreases, while WO_2 diffraction peaks emerge and strengthen. In the third stage (600–800 °C), WO_3 diffraction peaks nearly disappear, and strong signals from WO_2 and metallic W become evident (Figure S17a–c, Supporting Information). Throughout this process, the SiC component maintains its original crystal structure, showing only minor shifts in diffraction peak positions (Figure S17d, Supporting Information). This observation indicates that as the reduction temperature increases from 25 to 800 °C, the tungsten oxide component

undergoes progressive reduction from WO_3 to WO_{3-x}, and ultimately to WO_2 and W, while SiC remains structurally stable. Notably, the transformation trend observed in the XRD patterns correlates closely with the variation in BIEF intensity as a function of reduction temperature (Figures 4a,5c). Additionally, the consistent XRD behaviour between powder SW-T and single-crystal sc-SW-T samples (Figure S18, Supporting Information) suggests that surface and interface compositional changes are key factors enhancing BIEF intensity in the heterojunction.

Changes in the W 4f XPS spectra show a trend consistent with the XRD diffraction patterns in the range of the reduction temperature of 25–800 °C (Figure S19, Supporting Information). The binding energy of W continuously decreases from 25 to 500 °C, indicating a gradual reduction in the valence state of W^{6+}, and the formation of tungsten species with oxidation states lower than +6. Above 500 °C, different valence states corresponding to WO_2 and metallic W are observed.[61,62] These low-valence tungsten species are likely embedded at the SiC and WO_{3-x} heterojunction interface, contributing to the modified electronic structure of the heterojunction. The Si 2p XPS spectra display a noticeable shift in binding energy as the reduction temperature increases, initially rising to higher values and subsequently to lower energies, accompanied by the emergence of a new component labelled Si2 (Figure S20, Supporting Information). The Si2 feature is interpreted as an interfacial species resulting from the chemical interaction between WO_{3-x} and SiC, which promotes closer integration between the two semiconductors and strengthens the heterojunction interface.

Changes in the TEM and HRTEM images of SW-T samples with varying reduction temperatures further support the proposed evolution of the heterostructure (Figure S21, Supporting Information). Across the entire temperature range, the heterojunction interfaces in all SW-T samples remain well-defined and intimately contacted. Clear lattice fringes are observed on both sides of the interface, reflecting the distinct chemical compositions of constituent crystal phases. Specifically, the heterojunction consists of SiC and WO_{3-x} in the temperature range of 25–500 °C, transitions to a composite of SiC with WO_2 and residual WO_3 between 500–600 °C, and evolves into a multiphase interface comprising SiC, WO_2, W, and WO_3 above 600 °C, respectively.

Considering all these results, we conjecture that within the reduction treatment temperature range of 25–800 °C, the interface composition of the SW-T heterojunction undergoes a continuous transformation: starting from SiC@WO_3 (with interfacial Si-O-W bonds), progressing through an oxygen-deficient SiC@WO_{3-x} ($1 < x < 0$) (with mixed W^{5+} /W^{6+} valence states), and ultimately forming a composite interface of SiC@WO_2/WO_3 that may also incorporate metallic W. This evolution in interfacial chemical composition is responsible for the observed changes in BIEF intensity across the temperature range.

To further understand the relationship between interfacial evolution and charge behaviour, we performed Density functional theory (DFT) simulations on four heterostructure models: SiC@WO_3, SiC@WO_2 /WO_3 (with thinner and thicker WO_2 layers, respectively), and SiC@WO_2 /W/WO_3. As shown in **Figure** 7a–d, significant charge redistribution occurs at heterojunction interfaces: blue regions represent charge depletion, while green area indicates charge accumulation. Notably, the charge density decreases in the SiC region but increases at the WO_3 and WO_2 terminals, confirming the spontaneous electron transfer-induced localized charge rearrangement. It renders the SiC and WO_2 (WO_3) interfaces nucleophilic and electrophilic, respectively. As the WO_2 proportion increases, charge differential regions expand progressively. However, partial reduction of WO_2 to metallic W leads to a contraction of these charge differential zones. Atomic charge analysis further reveals that SiC transfers 0.83, 0.95, 1.01, and 0.89 electrons to the WO_3 side in the four models, respectively. It is confirmed that the reduction treatment can adjust the electron distribution between SiC and WO_3, thereby modifying the E_{bi} intensity. Both the change in the transferred electron numbers from SiC to WO_3 in SiC@WO_{3-x} heterojunction with the reduction treating temperature (Figure 7e) and the change in N_{EPN} of the photocatalytic reaction with the transferred electron numbers from SiC to WO_3 (Figure 7f) are basically consistent with the experimental results (Figures 4,5). This agreement highlights that the enhancement in photocatalytic activity is closely linked to interfacial charge transfer, which governs the formation and strength of the BIEF.

3.2. Reason for N_{EPN} Enhancement with the Reduction Temperature in the Photocatalytic Process

Although it is evident that reduction treatment modulates the E_{bi} intensity of the SiC@WO_3 heterojunction by regulating its interfacial species, the role of BIEF in promoting the transfer of photogenerated charge carriers and its overall contribution to the enhanced N_{EPN} value remains to be fully elucidated. To achieve this, KPFM was utilized to examine the spatial separation of photogenerated electrons and holes in the powder heterojunctions. The principle of this approach is as follows: a decrease in contact potential difference (CPD) under illumination compared to the darkness condition ($CPD_{darkness} > CPD_{illumination}$) at a given location indicates the presence of photogenerated electrons, whereas an increase ($CPD_{darkness} < CPD_{illumination}$) suggests the accumulation of holes.[63] The Surface Photovoltage (SPV) is the difference between CPD value under darkness and illuminated conditions,[49] as expressed in Equation (19), where $CPD_{illumination}$ and $CPD_{darkness}$ correspond to measurements taken at identical positions on the SiC and WO_3 components under dark and light conditions, respectively. A larger SPV value indicates a more efficient transfer of photogenerated electrons to SiC. This method thus provides quantitative means to verify whether the BIEF serves as the primary driving force for the migration of photogenerated electrons from WO_3 to SiC.

$$SPV = CPD_{illumination} - CPD_{darkness} \tag{19}$$

To minimize aggregation among nanocrystals, the ethanol dispersion of powder SW-T samples was diluted stepwise to a concentration below 0.02 ppm (Figure S22, Supporting Information). It thus allowed for the precise measurement of the surface potential difference at the interface between SiC and WO_3 under both dark and illuminated conditions, enabling the accurate calculation of SPV for different SW-T samples. For SW25, TEM imaging reveals a clear boundary between an irregular SiC nanoparticle (red dotted circle) and regular WO_3 nanoplates (blue

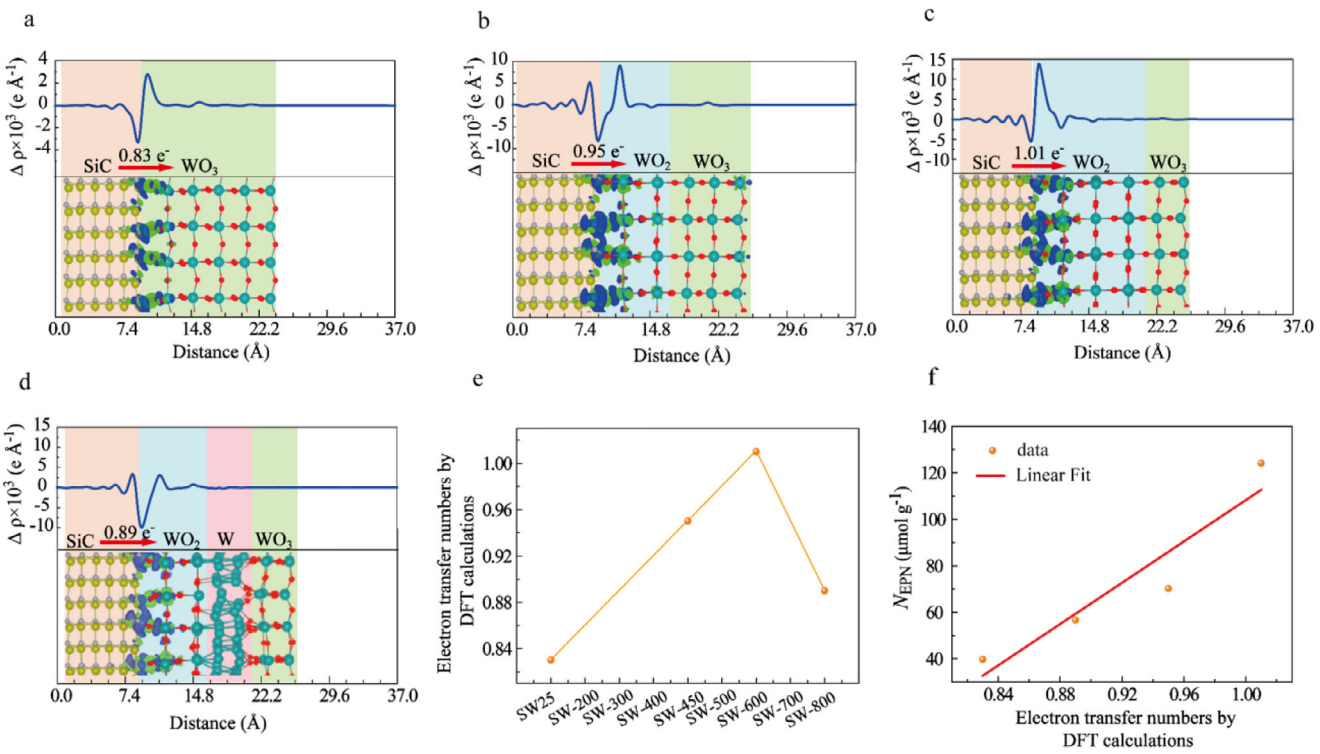

Figure 7. Calculated differential charge density distributions at the interface of (a) SiC@WO_3, b) SiC@WO_2/WO_3 (thinner WO_2 layer), c) SiC@WO_2/WO_3 (thicker WO_2 layer), and d) SiC@WO_2/W/WO_3 (The green and blue regions represent the electron accumulation and electron depletion, respectively. The blue lines display the planar-averaged electron density difference of heterostructures. The four rectangular boxes in orange, blue, pink, and green represent SiC, WO_2, W, and WO_3, respectively. e) Change in the calculated electron transfer numbers from SiC to WO_3 for SiC@WO_{3-x} with the reduction treating temperature. f) Photocatalytic reaction N_{EPN} value as a function of the calculated electron transfer numbers from SiC to WO_3 for the heterojunction.

dotted square) (Figure S23a_1, Supporting Information). The topography image further confirms distinct morphologies and a sharp contact interface (Figure S23a_2, Supporting Information). Under dark conditions, the surface potential of SiC (P_S) is measured to be 77 mV higher than that of WO_3 (P_W) (Figure S23a_3,a_4, Supporting Information), which agrees with the work function measured by the SKP method ($\phi_{WO3} > \phi_{SiC}$). Upon illumination, the potential of SW25 decreases, revealing the presence of photogenerated electrons (Figure S23a_5, Supporting Information).[49] The potential difference between the identical P_S and P_W points enlarges to 79.6 mV (Figure S23a_6, Supporting Information), demonstrating more efficient transfer of photogenerated electrons from WO_3 to SiC driven by the BIEF. The corresponding SPV value for SW25 was calculated to be 2.6 mV. Similar measurements were conducted across the SW-T series (Figure S23, Supporting Information). In all cases, signals assigned to photogenerated electrons are detected after light excitation, with consistent accumulation observed on the SiC side. The SPV value follows a volcanic curve with increasing reduction temperature, peaking at 600 °C for SW-600 before declining at higher temperatures (Figure S24, Supporting Information). A linear correlation is observed between built-in potential (V_{bi}) and SPV value (**Figure** 8a), confirming that a stronger BIEF enhances the transfer and accumulation of photogenerated electrons from WO_3 to SiC. Additionally, Figure 8b shows the linear correlation between SPV value and N_{EPN} value, which evidences that more efficient charge separation directly leads to higher photocatalytic activity. The proposed charge transfer pathways in SW25 and SW-600 were validated using Electron paramagnetic resonance (EPR) and the photodeposition experiments (Figures S25 and S26, Supporting Information). Enhanced electron-hole separation efficiency under stronger BIEF was further supported by Steady-state and Transient Photoluminescence, Photocurrent, and Electrochemical Impedance Spectroscopy (Figure S27, Supporting Information). The above results indicate that the stronger BIEF governs the migration efficiency of photogenerated electrons from the heterojunction interface to the photocatalyst surface, thereby determining the photocatalytic performance fundamentally.

4. Reason for the Difference in the N_{EPN} /V_{bi} of SW-T Samples from the N_{EPN} /E_{bi} of sc-SW-T Samples

As noted in Section 2.3, the fitted slope of the linear relationship between N_{EPN} and V_{bi} for powder of SiC@WO_3 (0.25 μmol g^{-1} kV^{-1}) differs from that between N_{EPN} and E_{bi} for single-crystal sc-SiC@WO_3 (0.16 μmol kV^{-1} cm). This discrepancy can be attributed to two main factors. First, the N_{EPN} /V_{bi} relationship does not consider the width (w) of the depletion region in the heterojunction, as discussed in Equation (3). In contrast, N_{EPN} /E_{bi} explicitly incorporates this spatial parameter. Second, the N_{EPN}

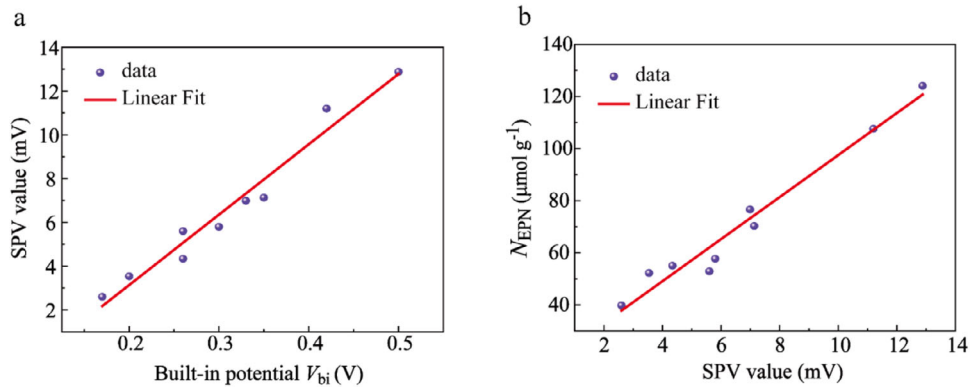

Figure 8. a) Correlation between V_{bi} and surface photovoltage (SPV) value. b) Correlation between SPV value and N_{EPN}.

value for powder samples is normalized by mass (μmol g^{-1}). In comparison, the N_{EPN} value for single-crystal samples is reported in absolute terms (μmol), due to challenges in precisely quantifying the effective photocatalytic dosage. This difference in normalization hinders a direct comparison of activity per unit interface or per active site. Therefore, for heterojunctions of the same chemical composition, it remains uncertain from the current data whether photocatalytic activity depends solely on the BIEF, as additional parameters, such as depletion layer width and accurately normalized activity metrics, must be consistently determined to enable a rigorous comparison. Nevertheless, extensive experimental evidence has demonstrated that the photocatalytic activity of heterojunction composites significantly surpasses the sum of the activities of the individual semiconductors, supporting the validity of the linear functional relationship for heterojunctions with identical chemical compositions but modified interfacial structures. On the other hand, for heterojunction photocatalysts composed of different chemical compositions, it remains an open question whether the BIEF intensity solely determines photocatalytic activity. We argue that since heterojunction materials are typically nanoscale materials, the photocatalytic activity cannot be merely determined by BIEF intensity. It is essential to consider that new chemical species formed at the heterojunction interface may act as active sites or cocatalysts, thereby contributing to the overall photocatalytic performance. The presence and quantity of such unconventional interfacial species cannot be overlooked in nanoscale heterojunctions.[9] In this context, the enhancement of photocatalytic activity of heterojunction materials is likely influenced not only by BIEF but also by the chemical species of heterojunction interfaces. This interplay between electronic and chemical effects warrants further in-depth investigation.

5. Conclusion

$SiC@WO_3$ can be constructed through the hydrothermal hydrolysis of tungstate precursors on SiC nanoparticles, followed by a reduction treatment to obtain the $SiC@WO_3$-T series. Two methods were adopted to determine the intensity of the built-in electric field quantitatively. i) The surface work function of the individual semiconductor components in the powder heterojunction was measured separately, and the built-in potential (V_{bi}) was calculated based on energy-band alignment diagram principles. ii) For single-crystal heterojunction samples, the potential distribution across the interface was directly mapped, and the BIEF intensity (E_{bi}) was derived through fitting. Both types of heterojunctions exhibited a linear relationship between the effective photoelectron number (N_{EPN}) involved in CO_2 reduction and the strength of E_{bi} or V_{bi}. Structural characterizations indicate that the presence of low-valence tungsten species at the $SiC@WO_3$ interface modulates the E_{bi} intensity. KPFM characterization further uncovers that a stronger E_{bi} enhances the transfer and accumulation of photogenerated electrons toward SiC, thereby improving charge separation efficiency and photocatalytic performance. These results establish the BIEF intensity as the key factor determining the photocatalytic CO_2 reduction activity in heterojunction systems. This study presents the first explicit physical mechanism for heterojunction photocatalysis, providing a rational strategy for designing more efficient artificial photosynthetic systems. Further investigation is needed to determine whether similar N_{EPN} /E_{bi} relationships apply to heterojunctions composed of other semiconductors.

Supporting Information

Supporting Information is available from the Wiley Online Library or from the author.

Acknowledgements

This research was financially supported by the National Natural Science Foundation of P.R. China (Grants Nos. 22372041 and 51702053), the Science & technology Key Plan Project of Fujian Province (Grants No. 2021YZ037005), and the Natural Science Foundation of Fujian Province (Grants No. 2025J01434).

Conflict of Interest

The authors declare no conflict of interest.

Data Availability Statement

Research data are not shared.

Keywords

heterojunction, interface modification, low valence-state tungsten element, quantification, the built-in electric field

Received: March 28, 2025
Revised: August 31, 2025
Published online:

[1] C. Fu, Z. Wan, X. Yang, J. Zhang, Z. Zhang, *J. Mater. Chem. A* **2024**, *12*, 28618.
[2] H. Zhu, R. Guo, C. Liu, H. Cui, M. Liu, W. Pan, *J. Mater. Chem. A* **2024**, *12*, 21677.
[3] J. Xue, M. Fujitsuka, T. Tachikawa, J. Bao, T. Majima, *J. Am. Chem. Soc.* **2024**, *146*, 8787.
[4] L. Wang, B. Zhu, J. Zhang, J. B. Ghasemi, M. Mousavi, J. Yu, *Matter* **2022**, *5*, 4187.
[5] Q. Wang, Z. Pan, *Nano Res.* **2022**, *15*, 10090.
[6] H. Song, S. Luo, H. Huang, B. Deng, J. Ye, *ACS Energy Lett.* **2022**, *7*, 1043.
[7] X. Tao, Y. Zhao, S. Wang, C. Li, R. Li, *Chem. Soc. Rev.* **2022**, *51*, 3561.
[8] Y. Shi, Z. Wang, Y. Song, J. C. Yu, L. Wu, *ChemCatChem* **2024**, *16*, 202401037.
[9] M. Lin, H. Chen, Z. Zhang, X. Wang, *Phys. Chem. Chem. Phys.* **2023**, *25*, 4388.
[10] C. Hu, *Modern Semiconductor Devices for Integrated Circuits*, Prentice Hall, Upper Saddle River, NJ, USA **2009**.
[11] B. Wilson, *Introduction to Physical Electronics*, Connexions, Rice University, Houston, TX, USA **2008**.
[12] X. Zhao, M. Liu, Y. Wang, Y. Xiong, P. Yang, J. Qin, X. Xiong, Y. Lei, *ACS Nano* **2022**, *16*, 19959.
[13] J. Qiu, X. Lei, B. Wang, H. Zhang, J. You, R. Guo, X. Liu, *Coord. Chem. Rev.* **2024**, *519*, 216115.
[14] C. Luo, C. Yang, J. Xie, X. Li, Y. Lin, S. Tong, S. He, *Chem. Eng. J.* **2024**, *497*, 155514.
[15] S. Li, Y. Lyu, J. Zheng, Z. Sofer, H. Zhou, *Flat Chem* **2024**, *47*, 100718.
[16] Z. Luo, X. Ye, S. Zhang, S. Xue, C. Yang, Y. Hou, W. Xing, R. Yu, J. Sun, Z. Yu, X. Wang, *Nat. Commun.* **2022**, *13*, 2230.
[17] S. Ida, A. Takashiba, S. Koga, H. Hagiwara, T. Ishihara, *J. Am. Chem. Soc.* **2014**, *136*, 1872.
[18] M. Hesari, X. Mao, P. Chen, *J. Am. Chem. Soc.* **2018**, *140*, 6729.
[19] H. Yang, C. Ni, X. Gao, S. Lin, X. He, L. Tian, Z. Li, *ChemSusChem* **2024**, *17*, 202400977.
[20] K. He, R. Shen, L. Hao, Y. Li, P. Zhang, J. Jiang, L. Xin, *Acta Phys.-Chim. Sin* **2022**, *38*, 2201021.
[21] B. Wang, X. Shang, J. Zhang, J. Shen, X. Wang, Z. Zhang, *Environ. Sci.: Adv.* **2023**, *2*, 132.
[22] M. Lin, M. Luo, Y. Liu, J. Shen, J. Long, Z. Zhang, *Chin. J. Catal.* **2023**, *50*, 239.
[23] H. Chen, X. Yang, M. Lin, D. Li, B. Wang, J. Shen, J. Long, W. Dai, X. Wang, Z. Zhang, *ACS Sustain. Chem. Eng.* **2023**, *11*, 18029.
[24] W. Xiao, J. Wang, J. Xiao, Y. Shen, X. Liang, T. Lv, *J. Mater. Chem. A* **2021**, *9*, 27442.
[25] X. Zhang, Z. Zhang, Y. Sun, X. Ma, F. Jin, F. Zhang, W. Han, B. Shen, S. Guo, *Rare Met.* **2024**, *43*, 3441.
[26] S. Adhikari, M. Murmu, D.-H. Kim, *Small* **2022**, *18*, 2202654.
[27] Y. Wang, Z. Zhang, L. Zhang, Z. Luo, J. Shen, H. Lin, J. Long, J. C. Wu, X. Fu, X. Wang, *J. Am. Chem. Soc.* **2018**, *140*, 14595.
[28] X. Dang, S. Wu, H. Zhao, *ACS Sustain. Chem. Eng.* **2022**, *10*, 4161.
[29] P. Li, J. Guo, X. Ji, Y. Xiong, Q. Lai, S. Yao, Y. Zhu, Y. Zhang, P. Xiao, *Chemosphere* **2021**, *282*, 130866.
[30] Q. Liu, F. Wang, H. Lin, Y. Xie, N. Tong, J. Lin, X. Zhang, Z. Zhang, X. Wang, *Catal. Sci. Technol.* **2018**, *8*, 4399.
[31] Z. Zhang, M. Haq, Z. Wen, Z. Ye, L. Zhu, *Appl. Surf. Sci.* **2018**, *434*, 891.
[32] C. Xiaolang, Z. Jingjing, L. Guisheng, Z. Dieqing, L. Hexing, *Energy Mater.* **2022**, *2*, 200001.
[33] X. Wu, H. Zhang, S. Xie, Y. Wang, *Chem Catalysis* **2023**, *3*, 100437.
[34] N. Lin, Y. Lin, X. Qian, X. Wang, W. Su, *ACS Sustain. Chem. Eng.* **2021**, *9*, 13686.
[35] D. Zhao, Y. Wang, C.-L. Dong, Y.-C. Huang, J. Chen, F. Xue, S. Shen, L. Guo, *Nat. Energy* **2021**, *6*, 388.
[36] G. Halek, I. Baikie, H. Teterycz, P. Halek, P. Suchorska-Woźniak, K. Wiśniewski, *Sens. Actuators, B* **2013**, *187*, 379.
[37] X. Fang, Y. Bando, U. K. Gautam, C. Ye, D. Golberg, *J. Mater. Chem.* **2008**, *18*, 509.
[38] M. Humayun, C. Wang, W. Luo, *Small Methods* **2022**, *6*, 2101395.
[39] Z. Zhang, J. T. Yates, Jr., *Chem. Rev.* **2012**, *112*, 5520.
[40] Z. Kiaee, S. K. Joo, *J. Nanosci. Nanotechnol.* **2018**, *18*, 1648.
[41] M. Razeghi, *Technology of Quantum Devices*, Springer, Boston, MA **2010**.
[42] B. V. Zeghbroeck, *Principles of semiconductor devices*, Online textbook, Boulder, Colorado **2011**.
[43] S. Sze, K. N. Kwok, *Physics of semiconductor devices*, 3rd Ed., John Wiley & Sons, Hoboken, NJ **2007**.
[44] U. K. Mishra, J. Singh, *Semiconductor Device Physics and Design*, Springer, Dordrecht, The Netherlands **2008**.
[45] H. Yang, *Mater. Res. Bull.* **2021**, *142*, 111406.
[46] C. P. C. V. Bernardo, R. A. M. Lameirinhas, J. P. de Melo Cunha, J. P. N. Torres, *Discov. Appl. Sci.* **2024**, *6*, 316.
[47] O. Lindberg, *Proceedings of the IRE* **1952**, *40*, 1414.
[48] Y. Gao, D. Zhu, H. An, P. Yan, B. Huang, R. Chen, F. Fan, C. Li, *J. Phys. Chem. Lett.* **2017**, *8*, 1419.
[49] R. Chen, Z. Ren, Y. Liang, G. Zhang, T. Dittrich, R. Liu, Y. Liu, Y. Zhao, S. Pang, H. An, C. Ni, P. Zhou, K. Han, F. Fan, C. Li, *Nature* **2022**, *610*, 296.
[50] Q. Zhou, Y. Guo, Z. Ye, Y. Fu, Y. Guo, Y. Zhu, *Mater. Today* **2022**, *58*, 100.
[51] L. Zhai, X. She, L. Zhuang, Y. Li, R. Ding, X. Guo, Y. Zhang, Y. Zhu, K. Xu, H. J. Fan, S. P. Lau, *Angew. Chem., Int. Ed.* **2022**, *61*, 202116057.
[52] X. Zhu, Y. Jia, Y. Liu, J. Xu, H. He, S. Wang, Y. Shao, Y. Zhai, Y. Zhu, *Angew. Chem., Int. Ed.* **2024**, *63*, 202405962.
[53] Y. Guo, W. Shi, Y. Zhu, *Eco Mat.* **2019**, *1*, 12007.
[54] Y. Guo, W. Shi, Y. Zhu, Y. Xu, F. Cui, *Appl. Catal. B* **2020**, *262*, 118262.
[55] Y. Sheng, W. Li, L. Xu, Y. Zhu, *Adv. Mater.* **2022**, *34*, 2102354.
[56] Y. Guo, S. Huang, Y. Guo, Z. Ye, J. Nan, Q. Zhou, Y. Zhu, *Appl. Catal. B* **2022**, *312*, 121388.
[57] J. Jing, J. Yang, W. Li, Z. Wu, Y. Zhu, *Adv. Mater.* **2022**, *34*, 2106807.
[58] S. Yue, G. Xiao, Q. Shi, X. Mu, M. Zhang, M. Xie, J. Cao, *Adv. Funct. Mater.* **2025**, https://10.1002/adfm.202503631.
[59] H. He, Y. Ren, L. Zhang, Y.-H. Zhu, R. Peng, T. Zeng, G. Hai, Y. Si, N. Li, X. Gao, Y. Zhu, *Nano Energy* **2025**, *142*, 111290.
[60] W. Liu, P. Wang, Y. Ao, J. Chen, X. Gao, B. Jia, T. Ma, *Adv. Mater.* **2022**, *34*, 2202508.
[61] S. L. Wang, Y. L. Mak, S. Wang, J. Chai, F. Pan, M. L. Foo, W. Chen, K. Wu, G. Q. Xu, *Langmuir* **2016**, *32*, 13046.
[62] M. Katoh, Y. Takeda, *Jpn. J. Appl. Phys.* **2004**, *43*, 7292.
[63] B. Xia, B. He, J. Zhang, L. Li, Y. Zhang, J. Yu, J. Ran, S. Z. Qiao, *Adv. Energy Mater.* **2022**, *12*, 2201449.

WILEY-VCH

Supporting Information

Deciphering the quantitative relationship between the photocatalytic activity and the built-in electric field of heterojunction

Chengwei Qiu, Jinni Shen, Haifeng Li, Yuhua Zhong, Jianhan Lin, Qing Wu, Dongmiao Li, Bing Wang, Ying Wang, Xuxu Wang, Xianzhi Fu, Zizhong Zhang**

State Key Lab of Photocatalysis on Energy and Environment, College of Chemistry, Fuzhou University, Fuzhou 350116, PR China.

Email: t15067@fzu.edu.cn, z.zhang@fzu.edu.cn

Contents

Materials and methods

1. Materials and reagents

All chemical reagents were used without further purification in this experiment, including ethanol (C_2H_5OH), hydrochloric acid (HCl), glucose ($C_6H_{12}O_6$), sodium hydroxide (NaOH), Nitric acid (HNO_3), which were analytical reagent grade and obtained from Sinopharm Chemical Reagent Co., Ltd. Tetraethyl orthosilicate (TEOS), sodium tungstate dihydrate ($Na_2WO_4{\cdot}2H_2O$), Tungsten (metal basis) and tungsten oxide (metal basis) were analytical reagent grade and obtained from Aladdin Chemical Reagent Co., Ltd. Tungsten trioxide disk (99.99%) was purchased from ZhongNuo Advanced Material (Beijing) Technology Co., Ltd. All the above chemicals were used without further purification.

2. Synthesis of photocatalysts

Synthesis of SiC NPs. 6.4 mL of tetraethyl orthosilicate (TEOS) and 10.8 g of glucose ($C_6H_{12}O_6$) were added to a mixed solution containing 3 mL of deionized water, 2.4 mL of ethanol (C_2H_5OH), and 0.3 mL of 1 M hydrochloric acid (HCl) in sequence. The mixture was magnetically stirred at room temperature for 24 h until a homogeneous colloid formed. After being heated to 120 °C in an oven, the above colloid transformed into an aerogel. Then, the aerogel was treated at 1500 °C for 8 h under argon flow. The resulting solid was purified by heat treatment under air at 800 °C for 6 h, followed by washing with sodium hydroxide solution to remove redundant carbon and SiO_2.

Synthesis of SiC@WO_3 composites. Typically, a certain amount of SiC NPs and $Na_2WO_4{\cdot}2H_2O$ was added to a 100 mL Teflon-lined autoclave containing 20 mL of deionized water. The resulting mixture was ultrasonicated for 30 minutes and stirred for an additional 30 minutes before 60 mL of HNO_3 (2 M) was added to the above solution. After stirring for 2 h, the autoclave was sealed and heated to 180 °C for 6 h. When the autoclave naturally cooled to room temperature, the product was washed with deionized water and dried at 60 °C in air. The above product was further calcined in air at 500 °C for 2 h and then ground into fine powder. The loading amount of WO_3 was set at 60%, representing the mass percentage of WO_3 in the resulting SiC@WO_3 sample. A pure WO_3 sample was synthesized in the same route except without the addition of SiC.

Synthesis of SiC@WO_3-T composites. The SiC@WO_3-T samples were obtained by static hydrogen reduction treatment of the SiC@WO_3 at different temperatures (T). Briefly, the SiC@WO_3 sample was placed in a conventional glass and quartz vacuum system, evacuated to a pressure of 0.2 Pa, and then purged with pure hydrogen. This process was repeated 6 times to eliminate residual oxygen, and then the sample was heated to the desired

temperature (T °C) at a rate of 5 °C min^{-1} and held for 2 h. According to the treatment temperature, the as-prepared samples are denoted as SW-T (T = 200, 300, 400, 450, 500, 600, 700, and 800 °C). For comparison, unmodified SiC@WO_3 is denoted as SW25. The pristine SiC and WO_3 samples were also treated similarly with hydrogen within the same temperature range and designated as SiC-T and WO_3-T, respectively.

Synthesis of sc-SiC@WO_3 and sc-SiC@WO_3-T samples. The pristine sc-SiC@WO_3 sample was obtained by sputtering WO_3 films onto a SiC single crystal (sc-SiC) substrate using the magnetron sputtering deposition method with a commercial sputtering system (SD-650MH, VPI Company). A stoichiometric tungsten trioxide disk (99.99% purity) was used as the target. The Radio frequency sputtering power was kept constant at 80 W. The target-substrate distance was 140 mm. Sputtering deposition was carried out under a 3 Pa pressure of an Ar atmosphere at a WO_3 film growth rate of 112 nm h^{-1}. The SiC single crystal substrate (10 × 10 mm) was partly covered by a photomask, and only a part of the SiC surface was sputtered with WO_3 films. The thickness of the sputtered WO_3 films was about 890 nm, measured by a 3D profiler (Bruker, Dektak XT, Germany) (Figure S12). The obtained films were annealed at 500 °C for 2 h in the air to improve their crystallinity. The as-obtained sc-SiC@WO_3 samples (sc-SW25) were then reduced under a hydrogen atmosphere as mentioned above, and sc-SiC@WO_3-T (T=200, 300, 400, 450, 500, 600, 700, and 800 °C) (sc-SW-T) samples were respectively prepared. The as-prepared sc-SW25 and sc-SW-T samples were sliced to expose the clean cross-section for potential images (Figure S14). Briefly, a notch was first made on the SiC side without a WO_3 film, and then the sample was sliced from the same side. The prepared sample was vertically fixed on a substrate using silver paste, with the interface plane of the heterojunction vertically aligned. To accurately obtain the band alignments, only the substrate was grounded. And therefore, the obtained work function will be normalized by the substrate [*J. Phys. Chem. Lett*. 2017, 8, 1419.]

3. Physicochemical characterizations

Powder X-ray diffraction (XRD) patterns were recorded with Ni-filtered Cu Kα radiation at 40 kV and 40 mA on a Bruker D8 Advance X-ray diffractometer. UV-Vis diffuse reflectance spectra (DRS) were generated using a Varian Cary 500 scanning spectrophotometer with $BaSO_4$ as the internal reflectance standard. Visible Raman spectra were taken on a Thermo Fisher DXR3 Raman microscope with an excitation wavelength of 532 nm. The scanning electron microscopy (SEM) images were taken on a Verios G4 scanning electron microscope. Transmission electron microscopy (TEM) and high-resolution TEM (HRTEM) images were obtained using a JEOL model JEM-2010 EX instrument with an accelerating voltage of 200 kV. X-ray photoelectron spectroscopy (XPS) and ultraviolet

photoelectron spectroscopy (UPS) were performed on an ESCALAB 250 XPS System with a monochromatized Al Kα X-ray source (15 kV, 200 W, 500 mm, pass energy = 20 eV). All binding energies were calibrated to the C 1s peak at 284.8 eV of surface adventitious carbon. Photoluminescence spectra (PL) were recorded at room temperature on a fluorescence spectrophotometer (Fluorolog-3). Fluorescence lifetime was determined by recording the time-resolved fluorescence emission spectra on a Deltapro Fluorescence Lifetime System. N_2 adsorption-desorption isotherm characterizations were conducted on a Micromeritics ASAP-3020 under liquid nitrogen conditions (-196 °C). Electron paramagnetic resonance (EPR) spectra were recorded on a Bruker A300 spectrometer (microwave frequency of 9.86 GHz, modulation amplitude of 3 G, modulation frequency of 100 kHz, microwave power of 6.37 mW) at 25 °C. The radical signals were recorded under illumination with a 300 W Xenon lamp with 5,5-dimethyl-1-pyrroline N-oxide (DMPO) as a spin-trapping agent. Photocurrent and electrochemical impedance spectroscopy were carried out on a conventional three-electrode electrochemical cell consisting of a working electrode (sample), a counter electrode (platinum foil), and a reference electrode (Ag/AgCl electrode with 3.0 M KCl). Light on/off short-circuit photocurrent response curve was measured by the CHI-660D workstation (CH Instrument), and the sodium sulfate electrolyte solution (0.2 M) was used as an electrolyte solution with a 300 W Xenon lamp as the irradiation source. Electrochemical impedance spectroscopy (EIS) was performed using an electrochemical analyzer (Zahner, Germany) in a three-electrode cell, with a 0.5 M KCl solution containing 5.0 mM $K_3[Fe(CN)_6]/K_4[Fe(CN)_6]$ as the electrolyte. Mott-Schottky plots were measured using a Bio-Logic workstation (SAS SP-300) in a 0.2 M Na_2SO_4 solution, with test frequencies of 500 Hz, 1000 Hz, and 1500 Hz, respectively. The voltage range of the Mott-Schottky plots test was -0.5 V to 1.5 V. Before use, FTO glasses were immersed in a mixture solution of acetone, ethanol, and water, and then sonicated for 1 h to remove impurities. Then, 5 mg of photocatalyst powder was dispersed in 0.5 mL of N,N-dimethylformamide (DMF) and treated with ultrasound to form a homogeneous slurry. After that, 10 μL of the slurry was spread onto the conductive surface of the FTO glass to create a photocatalyst film with an area of 0.28 cm^2 and was then dried at room temperature. The uncoated parts of the FTO glass were isolated with an epoxy resin.

4. Photocatalytic activity measurement

Photocatalytic reduction of CO_2 with H_2O vapor was carried out in a 40 mL Schlenk flask reactor with a silicone rubber septum under atmospheric pressure at ambient temperature (25 °C). A 300 W commercial Xe lamp (Microsolar 300, Beijing Perfectlight Technology Co., Ltd.) serves as the light source, positioned vertically outside

the reactor. The lamp is equipped with an optical filter ($\lambda \geq 420$ nm) to cut off the ultraviolet light. Typically, a certain amount of photocatalyst was loaded into the reactor. Before the illumination reaction, the reactor was evacuated using a mechanical pump and then filled with pure CO_2 gas at atmospheric pressure. This evacuation-filling operation was repeated three times. Finally, 20 μL of pure water was injected into the reactor through the silicone rubber septum by a microsyringe. The photocatalytic reaction was typically performed for 3 h. The stability test was performed for 5 h per cycle. The reaction system was evacuated after each 5 h and refilled with CO_2 and pure water. After the irradiation, the gas products were analyzed using an Agilent GC-7890B gas chromatograph equipped with an FID detector, a TCD detector, and a chromatographic column (TDX-01).

5. KPFM measurement

Atomic Force Microscopy (AFM) and Kelvin Probe Force Microscopy (KPFM) images were obtained using a Bruker Dimension Icon atomic force microscope. An amplitude-modulated (AM-KPFM) surface potential mode was performed in lift mode with drive routing to the tip. The model of the tip is MESP-V2, featuring a magnetic CoCr coating on the front side, with a resonance frequency of fr = 75 kHz and a force constant of k = 3 N m^{-1}. The target amplitude is set at 500 mV. In the lift mode, the topography and surface potential signals are sequentially recorded. In the first scan, the sample's topography is acquired along a scan line. Then, a second scan is executed along the first scan profile at a lift height of 138.1 nm from the first scan height, recording the variations in local surface potential. For KPFM measurement under illumination, a 300 W Xenon lamp was used to focus on the sample. According to the instruction manual, under the driving routine to tip setting in the software, the locations with higher *CPD* values have smaller work functions.

6. Photoinduced redox probe experiment

A photoinduced redox probe experiment was implemented to verify the transport paths of photogenerated electrons and holes in SW25 and SW-600 samples by selectively photo-depositing Au and MnO_2 on the samples. [*Adv. Mater.* 2023, 35, 2210374.] which occurs in the following Equation (S1) -(S2),

$$Au^{3+} + 3e^- \rightarrow 3Au \downarrow \quad \text{(S1)}$$

$$Mn^{2+} + 2H_2O + 2h^+ \rightarrow MnO_2 \downarrow + 4H^+ \quad \text{(S2)}$$

In detail, $HAuCl_4$ and $(CH_3COO)_2Mn$ precursors were used to deposit Au (1 wt.%) and MnO_2 (7 wt.%), and methanol and $NaIO_3$ aqueous solution were used as hole and electron sacrificial reagents, respectively. After irradiation for 1 h, the samples were washed and dried in a vacuum oven at 60 °C for 12 h.

7. Calculation methods

Density functional theory (DFT) calculations were carried out using the PWmat software package. [*Comput. Phys. Commun. 2013, 184, 9.*] The exchange-correlation functional was described within the generalized gradient approximation (GGA) framework, specifically employing the revised Perdew-Burke-Ernzerhof (PBE) functional. [*Phys. Rev. Lett*. 1996, 77, 3865.] Electron-ion interactions were modeled using the norm-conserving SG15 pseudopotentials, [*J. Comput. Phys*. 2013, 251, 102.] and a kinetic energy cutoff of 60 Ry was applied for the plane-wave basis set. The Brillouin zone was sampled with a Γ-centered k-point mesh of 1 × 1 × 1. All atomic positions were fully relaxed until the maximum force on any atom was less than 0.05 $eV \cdot Å^{-1}$ and the total energy change between iterations was below 10^{-6} eV. To avoid spurious interactions between periodic images, a vacuum spacing of 20 Å was introduced in the supercell. The SiC (111) surface is constructed from a cubic phase with a lattice parameter of a = 4.35 Å, resulting in a surface unit cell parameter of a = 10.72 Å and b = 15.15 Å, which contains 72 C atoms and 72 Si atoms. The WO_3 (200) surface is constructed from a monoclinic phase, with unit cell parameters of a = 5.41 Å, b = 5.36 Å, and c = 7.72 Å. The structural parameters for the WO_3 (200) surface are a = 10.72 Å and b = 15.34 Å. The WO_2 (101) surface is based on a triclinic primitive cell, with unit cell parameters of a = 5.57 Å, b = 4.92 Å, c = 5.69 Å. The surface structural parameters for WO_2 (101) are a = 10.96 Å and b = 13.90 Å. The SiC@WO_3 heterojunction is formed by the combination of the SiC (111) thin sheet and the WO_3 surface. The SiC@WO_2/WO_3 heterostructure is constructed from the previously mentioned SiC (111) thin sheet along with WO_2 and WO_3 surfaces of varying thicknesses. A two-atom-thick metallic W (110) layer (lattice constants a = 9.01 Å, b = 12.75 Å) was employed as the structural counterpart of W formed by the high-temperature reduction of WO_2, thereby constructing the SiC@WO_2/W/WO_3 model.

Supplementary Figures

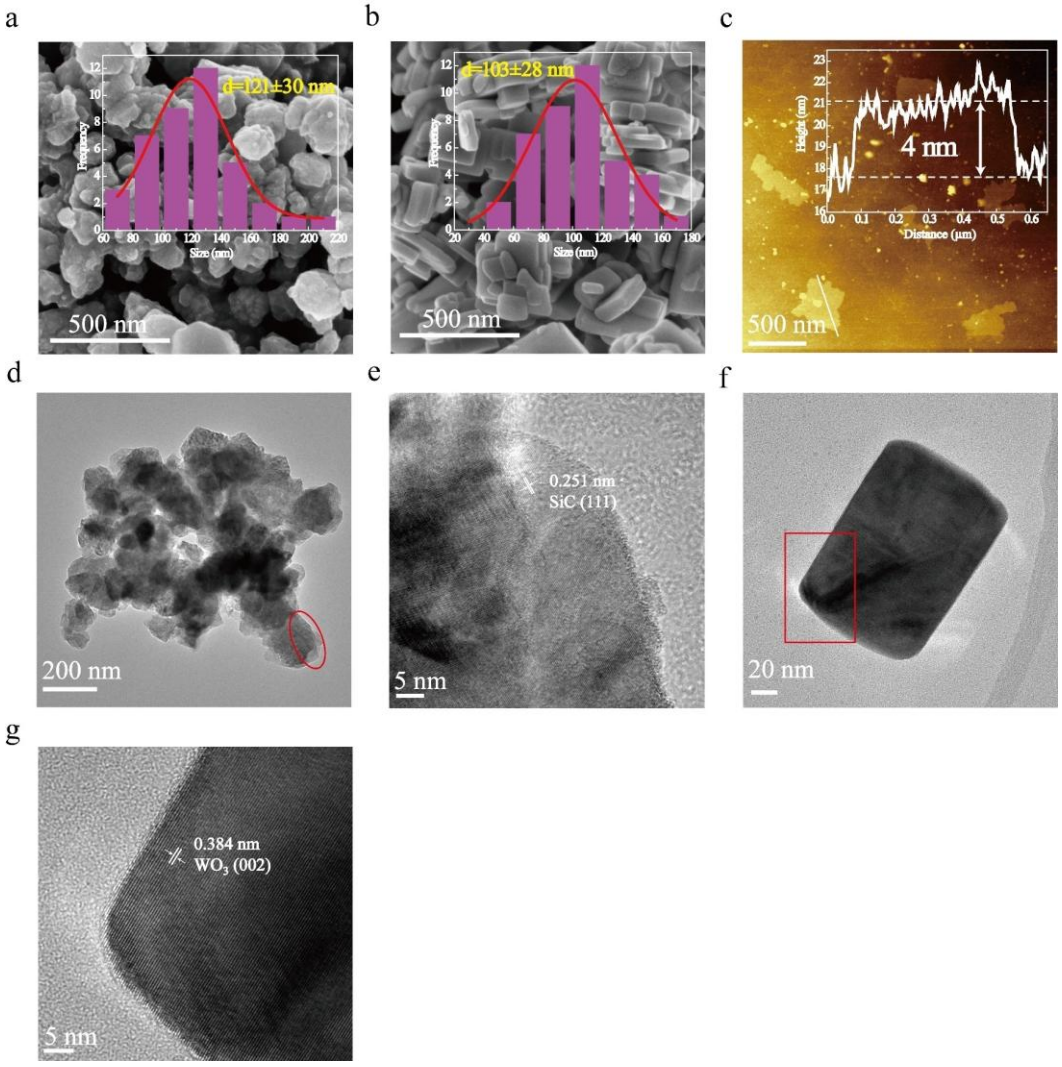

Figure S1. (a) and (b) SEM images of SiC and WO_3 with respective particle distribution inset. (c) AFM image of WO_3 and the height profile. (d) and (f) TEM images of nude SiC and WO_3. (e) and (g) HRTEM images of nude SiC and WO_3.

The pristine SiC exhibits an aggregated spherical morphology, whereas the naked WO_3 displays a piled nanoplate shape (S1a-c), which is further confirmed by their TEM images (S1d and S1f). The lattice fringes show interplanar spacing of 0.251 nm and 0.384 nm corresponding to the (111) and (002) facets of SiC [*J. Am. Chem. Soc*. 2018, 140, 14595.] and WO_3 [*J. Alloys Compd*. 2019, 783, 848.] respectively, which further affirms their phase structures (S1e and S1g).

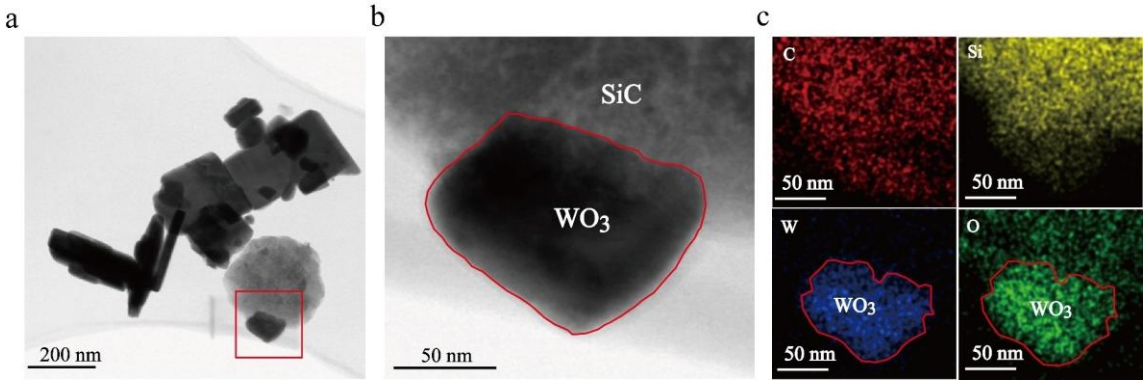

Figure S2. (a) TEM image of SW25, (b) the High-Angle Annular Dark-field scanning transmission electron microscope (HAADF-STEM) image, and (c) the respective mapping images of C, Si, W, and O in SW25.

The hybrid structure of SW25 shows that SiC nanoparticles and WO_3 nanoplates are intimately contacted (S2a). Furthermore, the energy dispersive spectroscopy (EDS) mapping profile of C, Si, and W, O elements in SW25 further indicates that WO_3 nanoplates are attached to the SiC nanoparticles in the heterostructure (S2b-c).

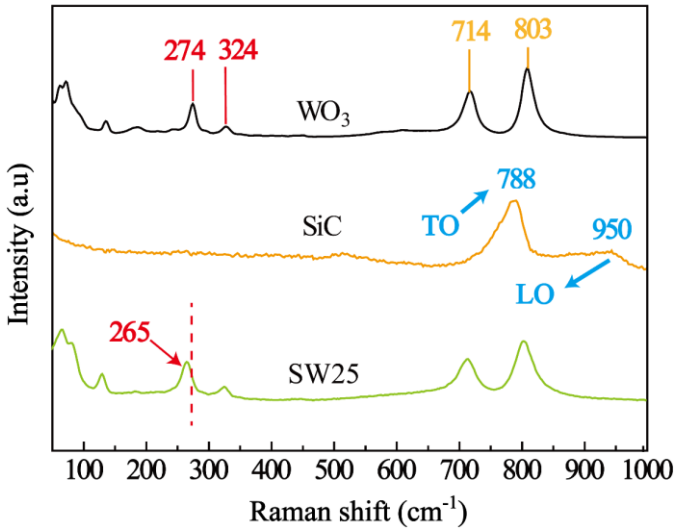

Figure S3. The Visible-Raman spectra of SiC, WO_3, and SW25 samples.

Raman bands of nude SiC at 788 and 950 cm^{-1} are characterized by the modes of transverse optical (TO) and longitudinal optical (LO) phonons of 3C-SiC (S3). [*J. Appl. Phys*. 2002, 91, 6066.] For pristine WO_3, the bands 274 and 324 cm^{-1} belong to the O-W-O bending modes, and the two peaks at 714 and 803 cm^{-1} belong to the O-W-O stretching modes. [*J. Raman Spectrosc*. 2007, 38, 176. *Appl. Surf. Sci*. 2018, 434, 891.] After coupling with SiC, the Raman bands of WO_3 are well observed in SW25, and the Raman band at 274 cm^{-1} shifts negatively to 265 cm^{-1}. Such a blue shift reflects the existing interaction between SiC and WO_3. [*Appl. Surf. Sci*. 2018, 434, 891.]

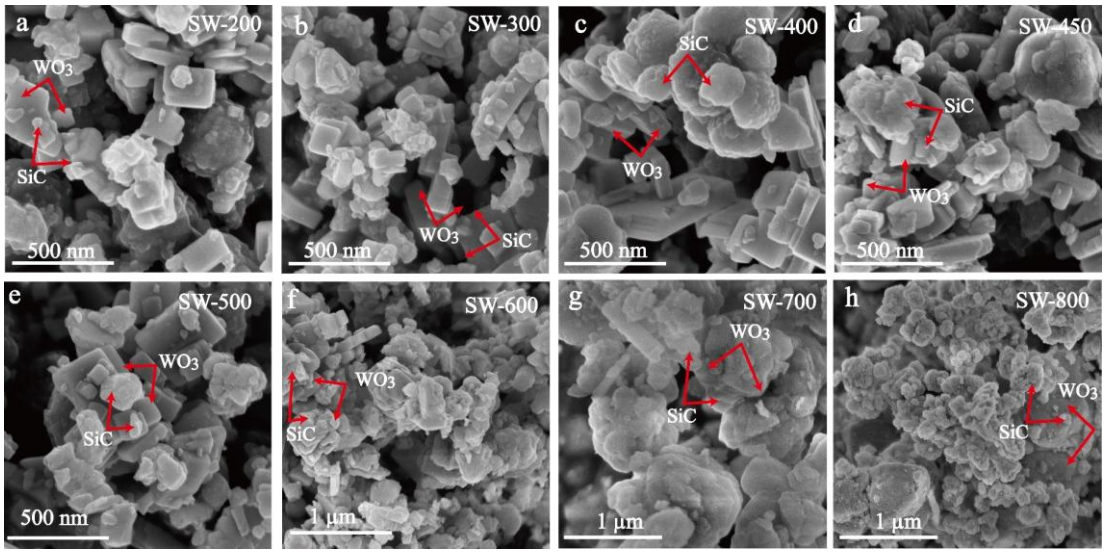

Figure S4. SEM images of samples: (a) SW-200, (b) SW-300, (c) SW-400, (d) SW-450, (e) SW-500, (f) SW-600, (g) SW-700, and (h) SW-800.

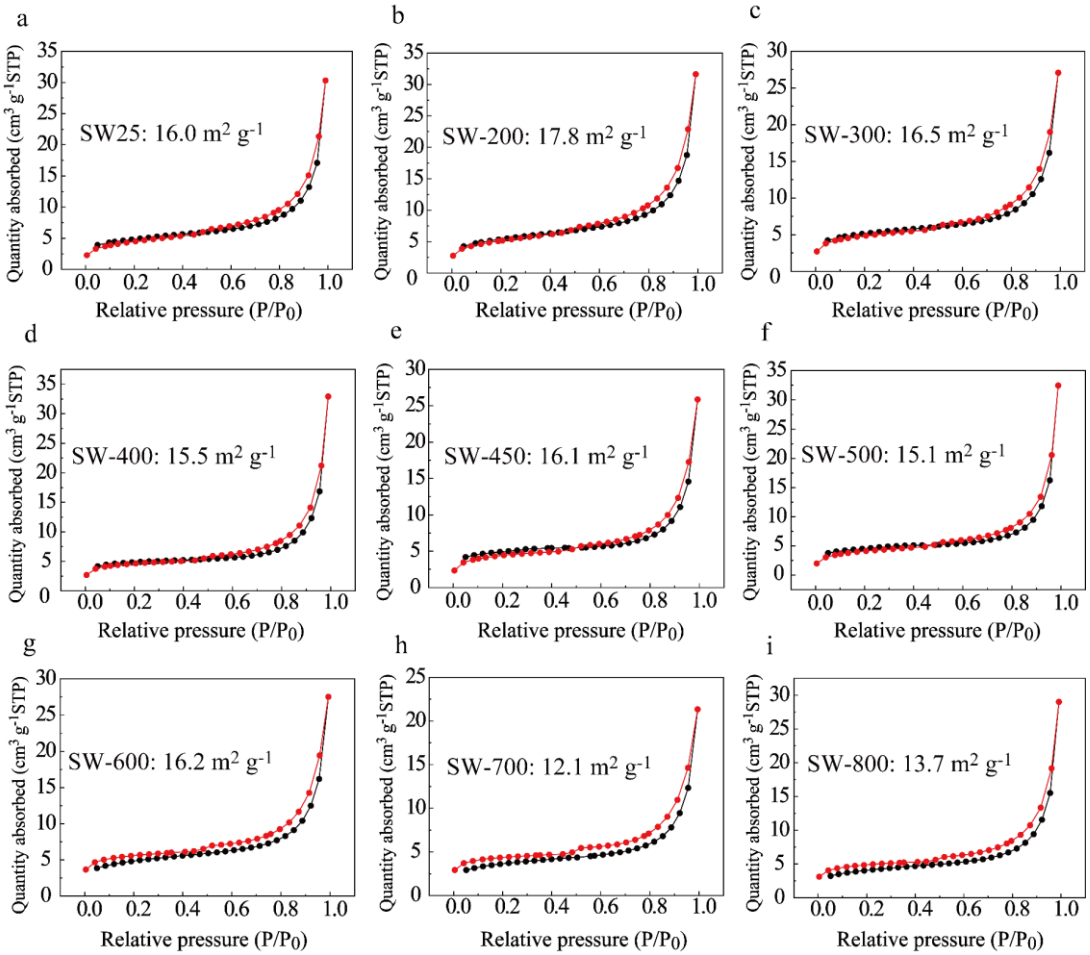

Figure S5. N_2 adsorption-desorption isotherms of samples: (a) SW25, (b) SW-200, (c) SW-300, (d) SW-400, (e) SW-450, (f) SW-500, (g) SW-600, (h) SW-700 and (i) SW-800.

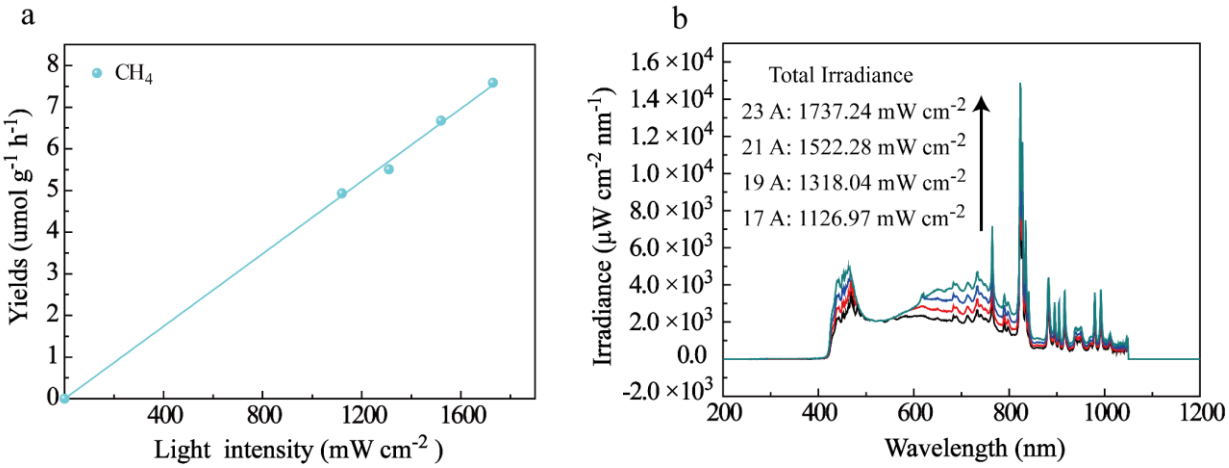

Figure S6. (a) CH_4 evolution rate on the SW-600 sample illuminated under different light intensities controlled by the working current of the Xe lamp. (b) The irradiance spectrum of a 300 W Xe lamp with an optical filter $\lambda \geq 420$ nm) under different working currents (17, 19, 21, and 23 A).

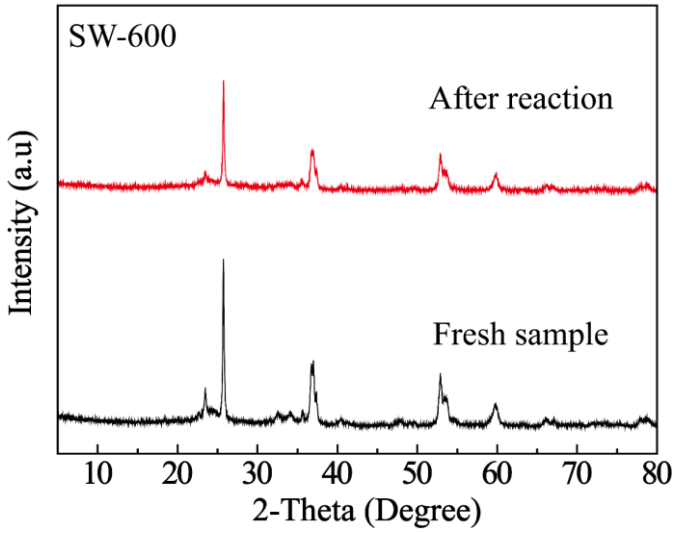

Figure S7. XRD patterns of the SW-600 sample before and after the photocatalytic reaction.

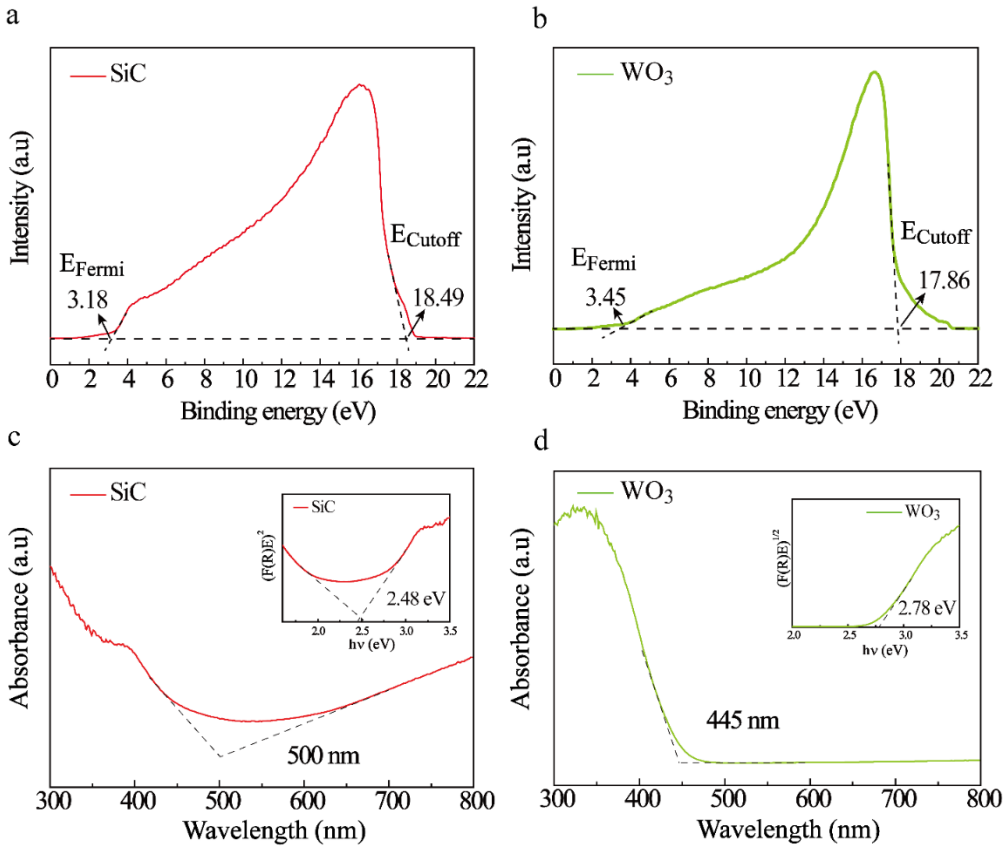

Figure S8. The UPS spectra of (a) SiC, (b) WO_3 samples. The UV–vis diffuse reflectance spectra and the inset Kubelka–Munk function-transformed spectra versus (*hv*) of (c) SiC, (d) WO_3 samples.

The E_{VB} of SiC and WO_3 was calculated to be -5.91 eV and -6.81 eV (vs. vacuum) (S8a-b) from Equation (S3),

$$E_{VB} = hv + E_{Fermi} - E_{Cutoff} \quad \text{(S3)}$$

Where *hv* denotes the He I excitation energy of 21.22 eV. [*Nat. Energy* 2021, 6, 388.] Further, we calculated their conduction band positions, combining with their band gap energy. The UV-vis DRS shows that nude SiC exhibits an optical response edge at *ca*. 500 nm. The absorption edge of WO_3 is at *ca*. 445 nm. The corresponding band gap energies (E_g) were obtained by the Kubelka−Munk in Equation (S4):

$$\alpha h\nu = A(h\nu - E_g)^n \quad \text{(S4)}$$

Where A, E_g, ν, *h*, and α are constant, the band gap energy, the light frequency, the Planck constant, and the absorption coefficient, respectively. n = 2 or 1/2 corresponds to the indirect band gap or direct band gap semiconductors, respectively. The band gap energies (E_g) of SiC and WO_3 were therefore determined to be 2.48 eV and 2.78 eV, respectively. [*ACS Appl. Mater. Interfaces* 2020, 12, 40176. *ACS Appl. Mater. Interfaces* 2017, 9,

40235.] Based on the conduction band potential and band gap energies calculated above, the E_{CB} of SiC and WO_3 was calculated by Equation (S5) to be -3.43 eV and -4.03 eV (vs. vacuum).

$$E_{VB} = E_g - E_{CB} \quad \text{(S5)}$$

Based on the relationship between the vacuum energy level (E_{vacuum}) and the RHE potential (E_{RHE}) in Equation (S6), the E_{CB} and E_{VB} of SiC and WO_3 vs. RHE were determined, and their band structures were summarized (S9 and Table S2). It shows that SiC satisfies the potential requirement to reduce CO_2 into CH_4 or CO. [*ACS Sustainable Chem. Eng*. 2021, 9, 13686.] At the same time, the water oxidation reaction into dioxygen can occur on WO_3.

$$E_{vacuum} = -E_{RHE} - 4.44\ eV \quad \text{(S6)}$$

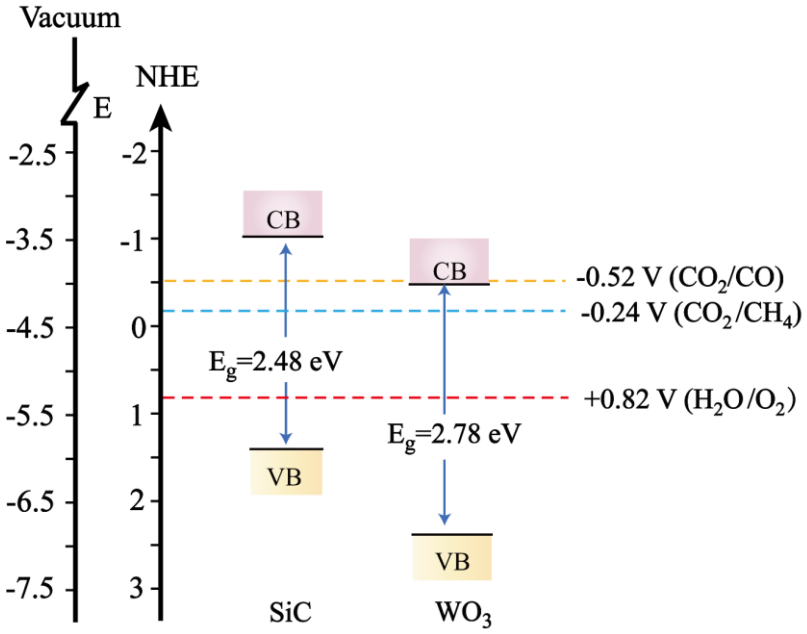

Figure S9. The band structures of SiC and WO_3 before contact.

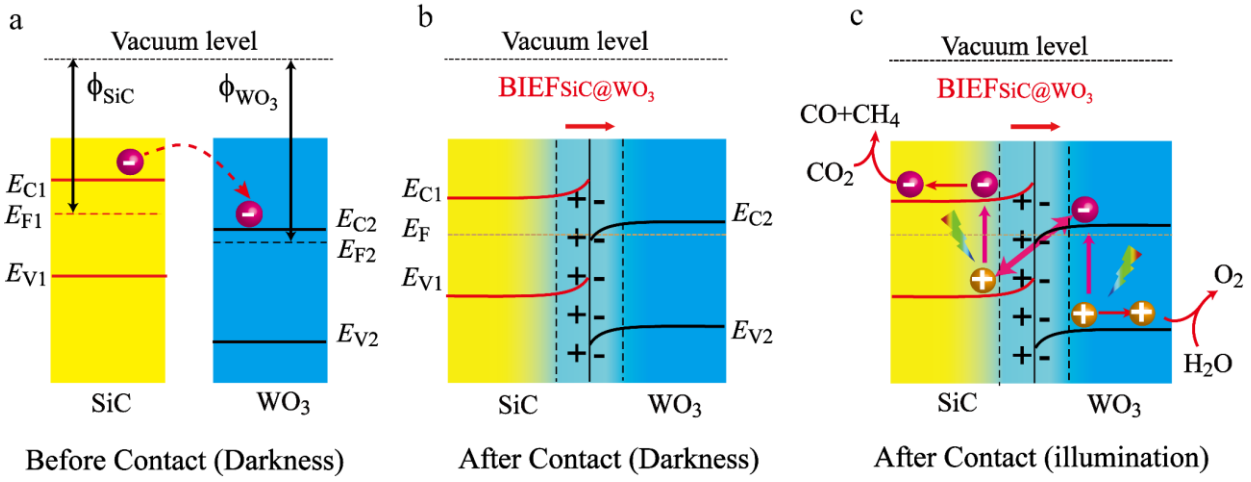

Figure S10. The energy-band diagrams of SiC and WO_3 before contact (a), after contact (b), and the possible electron transfer under illumination (c).

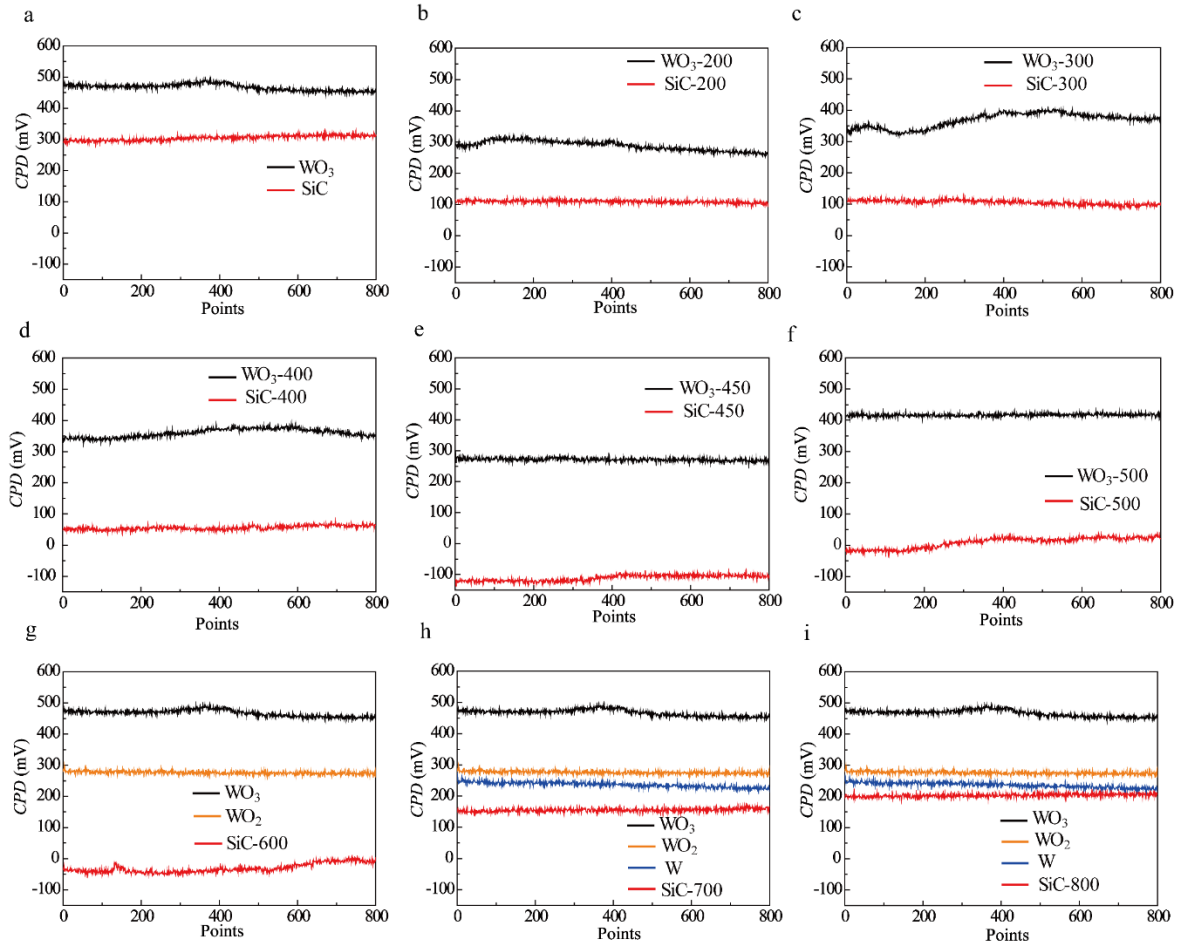

Figure S11. *CPD* value change of SiC-T and WO_3-T samples with reduction temperature (a)-(f). *CPD* value change of SiC-T with reduction temperature and *CPD* value of WO_3, WO_2, W samples (g)-(i).

Pristine WO_3 shows a higher work function value than SiC (S11a). As the reduction temperature increases from 200 to 500 °C, the built-in potential (V_{bi}) between SiC-T and WO_3-T gradually enlarges for SW-T samples (S11b-S11f). For the SW-600 sample, since WO_3 was partially reduced to WO_2, and the work function value of WO_2 lies between those of WO_3 and SiC-600, the V_{bi} between SiC-600 and WO_3 was calculated instead (S11g). For SW-700 and SW-800 samples, the work functions of commercial WO_3 and W were measured separately. Since the work function values of WO_2 and W are located between those of SiC-700 and WO_3, the V_{bi} between SiC-700 and WO_3 or between SiC-800 and WO_3 was calculated instead (S11h-i).

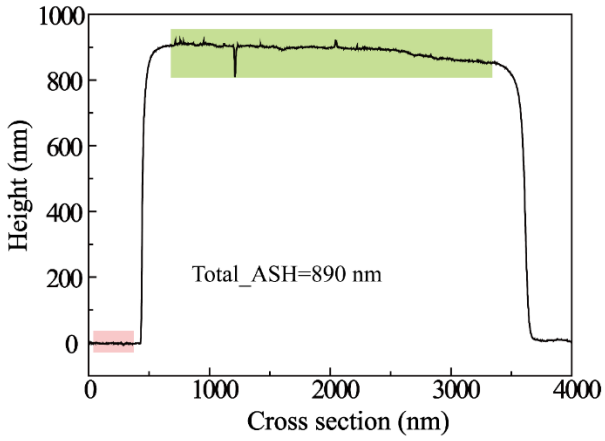

Figure S12. Measurement of the WO_3 film thickness on the sc-SiC substrate.

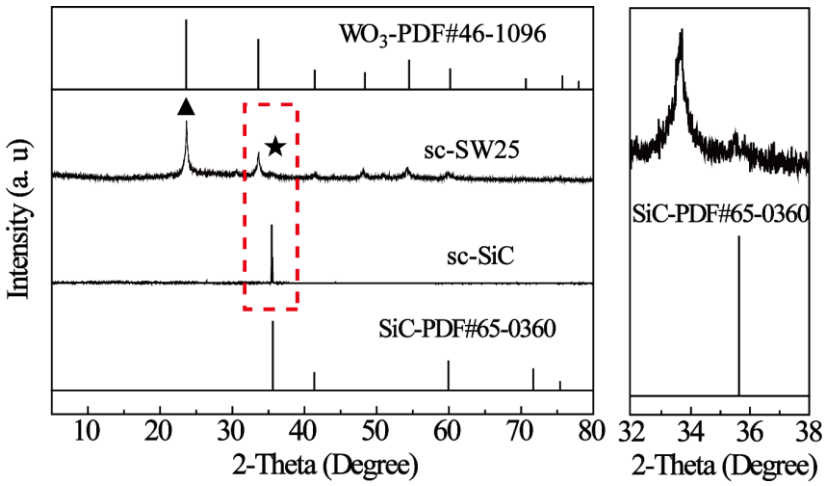

Figure S13. XRD patterns of sc-SiC and sc-SW25 samples.

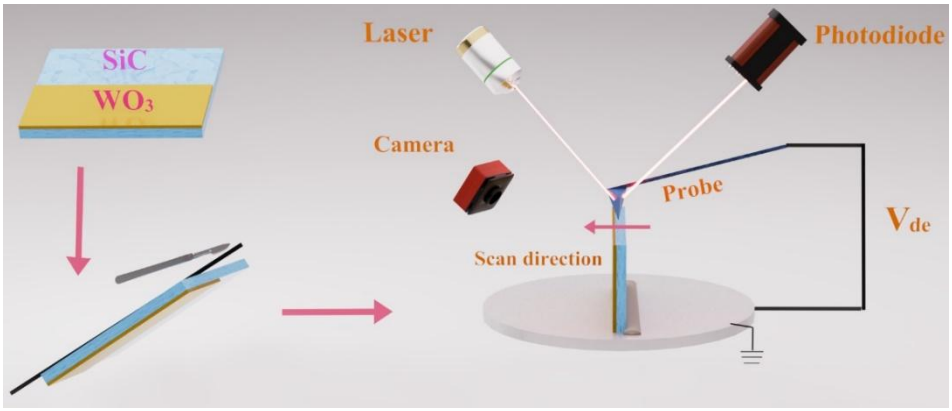

Figure S14. Schematic measurement of the BIEF intensity.

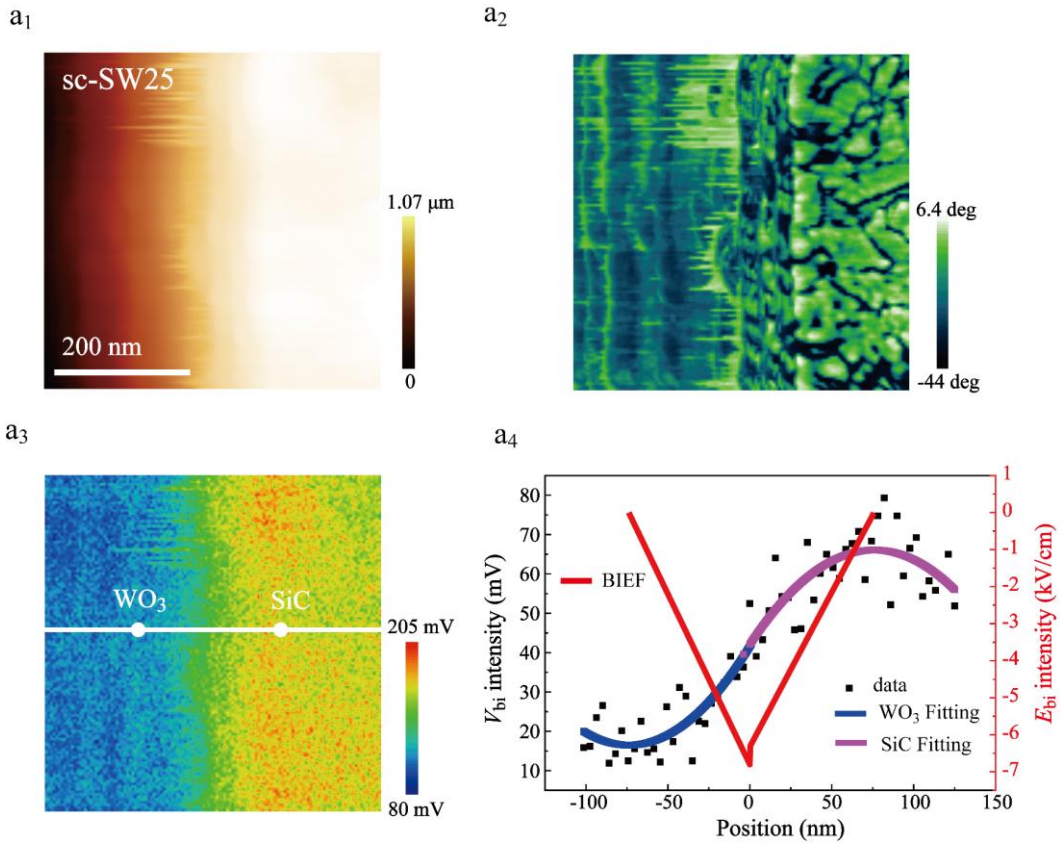

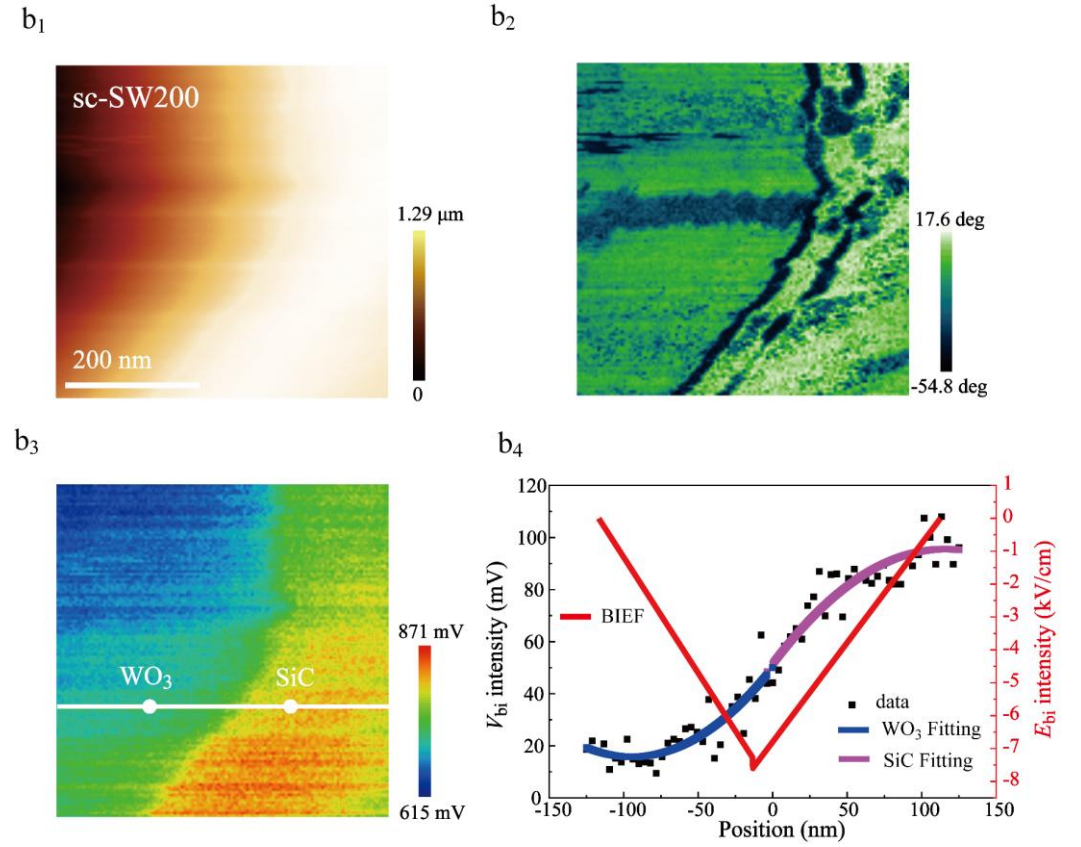
b1
sc-SW200
1.29 μm
200 nm
0
b2
17.6 deg
-54.8 deg
b3
WO3
SiC
871 mV
615 mV
b4
BIEF
data
WO3 Fitting
SiC Fitting
Vbi intensity (mV)
Ebi intensity (kV/cm)
Position (nm)
c1
sc-SW300
1.33 μm
200 nm
0
c2
6.4 deg
-44.6 deg
c3
WO3
SiC
748 mV
535 mV
c4
BIEF
data
WO3 Fitting
SiC Fitting
Vbi intensity (mV)
Ebi intensity (kV/cm)
Position (nm)

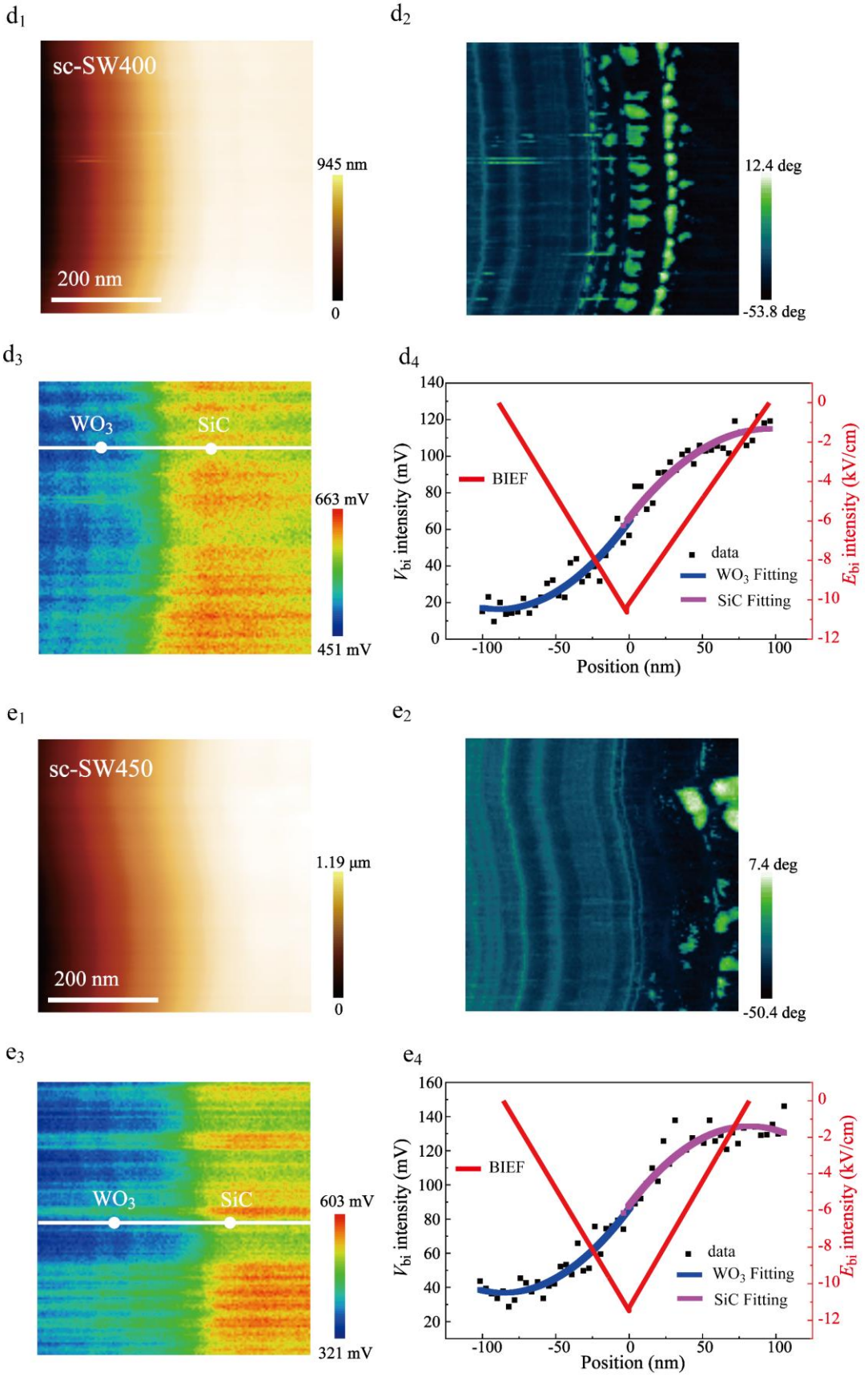
d1
sc-SW400
945 nm
0
200 nm
d2
12.4 deg
-53.8 deg
d3
WO3
SiC
663 mV
451 mV
d4
BIEF
data
WO3 Fitting
SiC Fitting
Vbi intensity (mV)
Ebi intensity (kV/cm)
Position (nm)
e1
sc-SW450
1.19 μm
0
200 nm
e2
7.4 deg
-50.4 deg
e3
WO3
SiC
603 mV
321 mV
e4
BIEF
data
WO3 Fitting
SiC Fitting
Vbi intensity (mV)
Ebi intensity (kV/cm)
Position (nm)

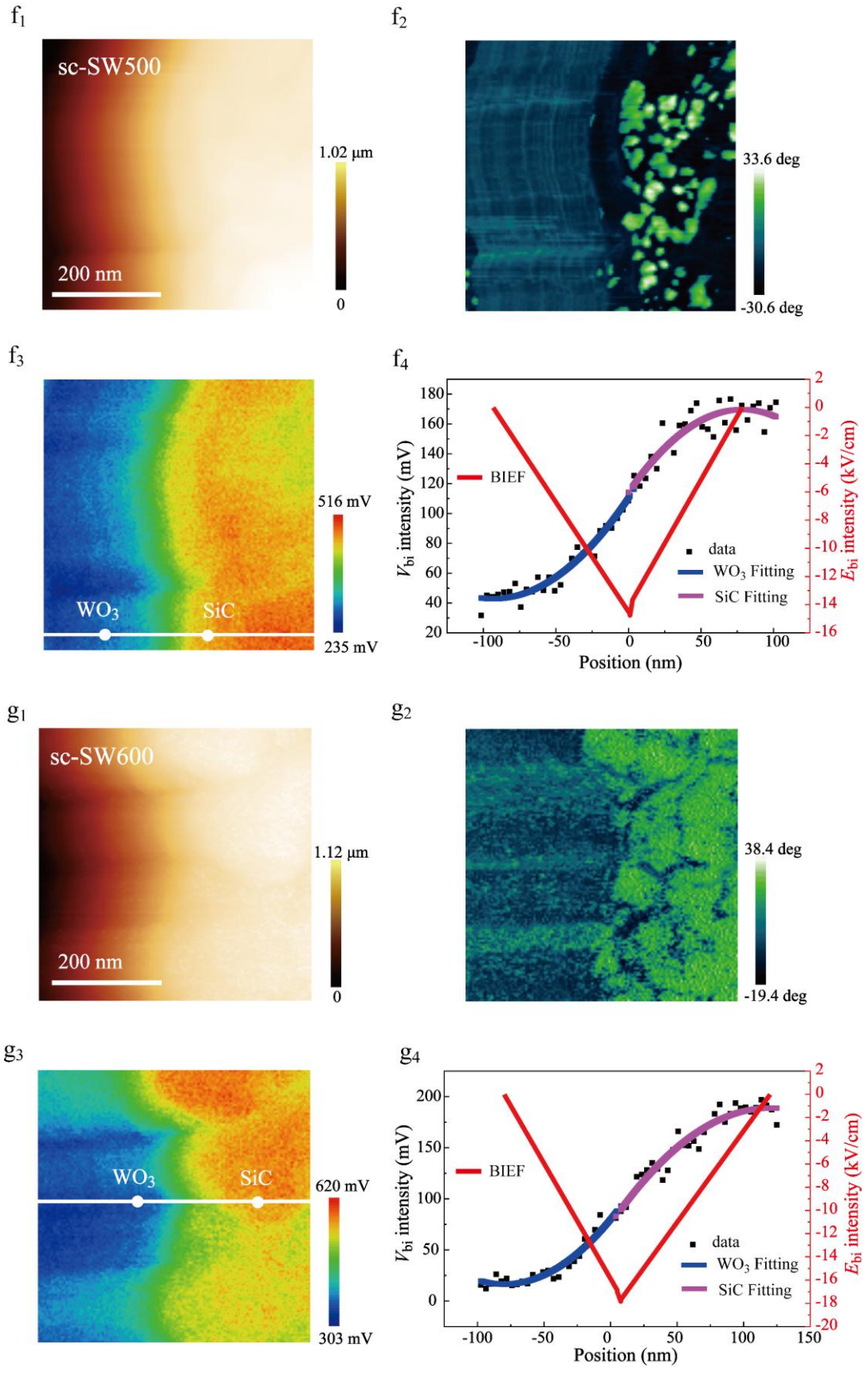
f1
sc-SW500
1.02 μm
0
200 nm
f2
33.6 deg
-30.6 deg
f3
WO3
SiC
516 mV
235 mV
f4
BIEF
data
WO3 Fitting
SiC Fitting
Vbi intensity (mV)
Ebi intensity (kV/cm)
Position (nm)
g1
sc-SW600
1.12 μm
0
200 nm
g2
38.4 deg
-19.4 deg
g3
WO3
SiC
620 mV
303 mV
g4
BIEF
data
WO3 Fitting
SiC Fitting
Vbi intensity (mV)
Ebi intensity (kV/cm)
Position (nm)

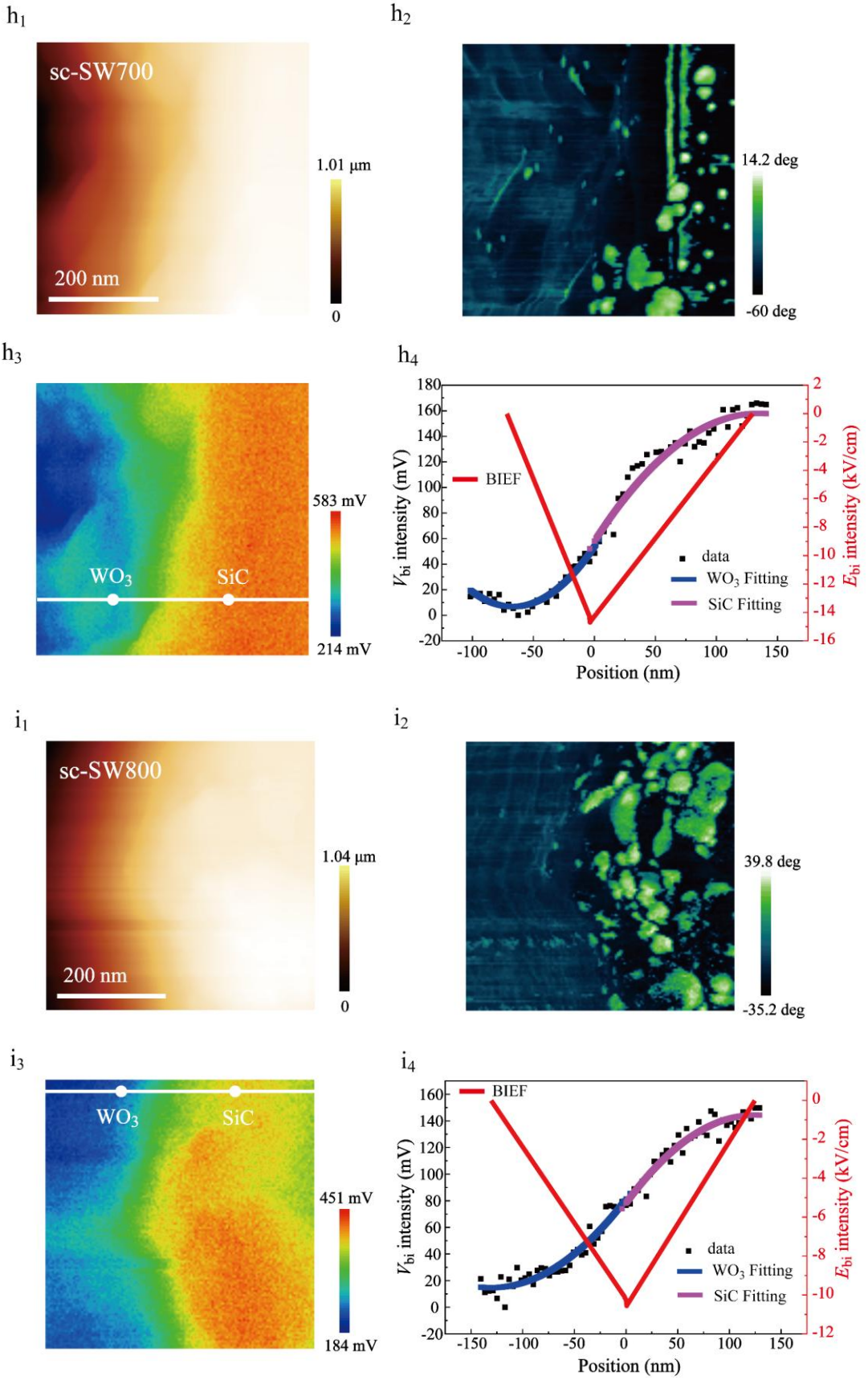
h1
sc-SW700
1.01 μm
0
200 nm
h2
14.2 deg
-60 deg
h3
583 mV
214 mV
WO3
SiC
h4
BIEF
data
WO3 Fitting
SiC Fitting
Vbi intensity (mV)
Ebi intensity (kV/cm)
Position (nm)
i1
sc-SW800
1.04 μm
0
200 nm
i2
39.8 deg
-35.2 deg
i3
451 mV
184 mV
WO3
SiC
i4
BIEF
data
WO3 Fitting
SiC Fitting
Vbi intensity (mV)
Ebi intensity (kV/cm)
Position (nm)

Figure S15. For sc-SW25 and sc-SW-T samples with reduction temperature (T): (a_1)-(i_1) Change of the topography images. (a_2)-(i_2) Change of the phase images across the junction interface. (a_3-i_3) Change of the V_{bi} value of the cross-section profile. (a_4)-(i_4) Change of the V_{bi} value distribution and fitting within the SiC and WO_3 heterojunction interface and the E_{bi} intensity distribution across the heterojunction interface.

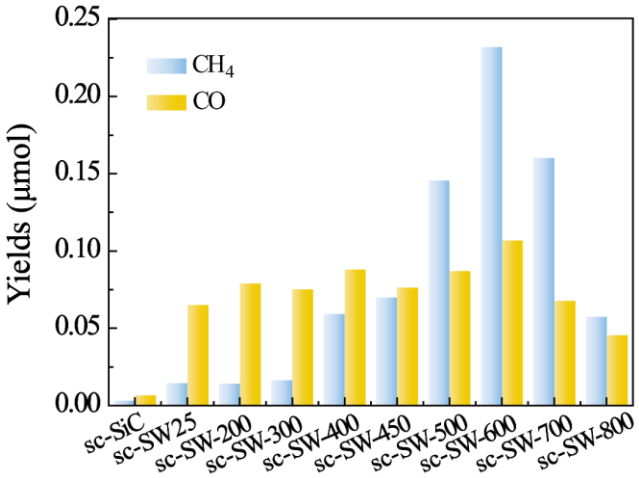

Figure S16. Photocatalytic CO_2 reduction activities of sc-SiC, sc-SW25, and their change with reduction temperature (T) in sc-SW-T samples.

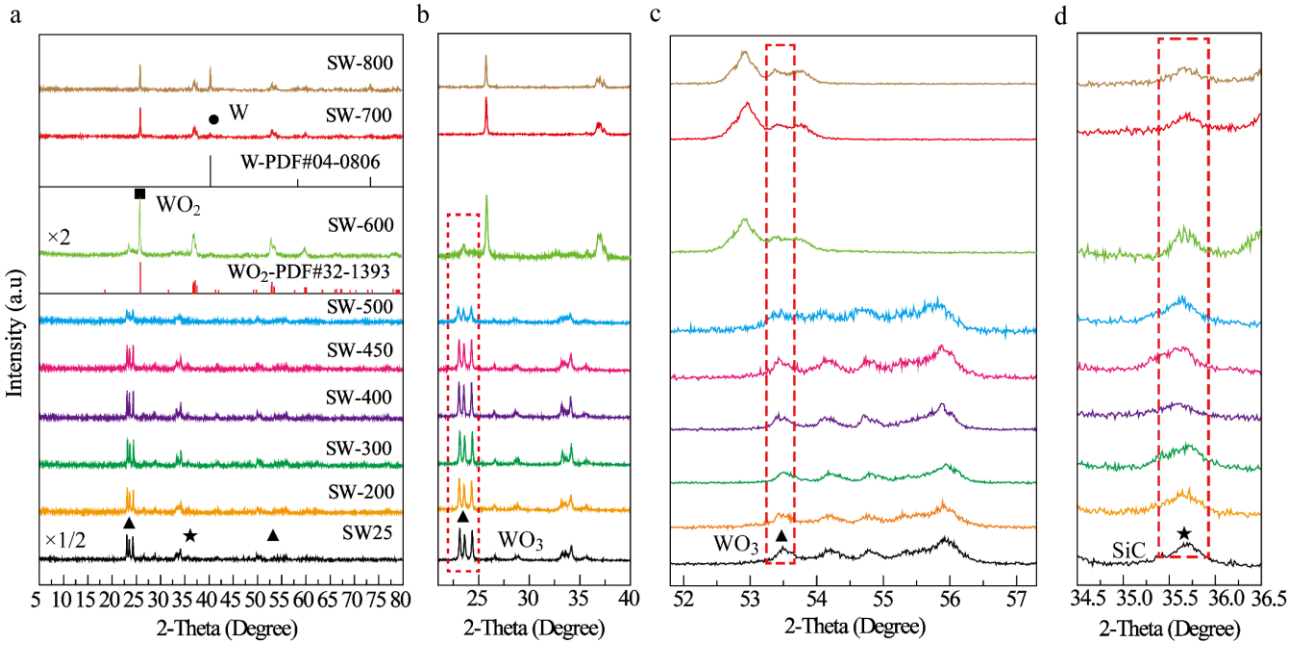

Figure S17. Change of the XRD patterns of SW-T samples with reduction temperature (a) and the corresponding zoom regions for WO_3 (b)-(c), and for SiC (d).

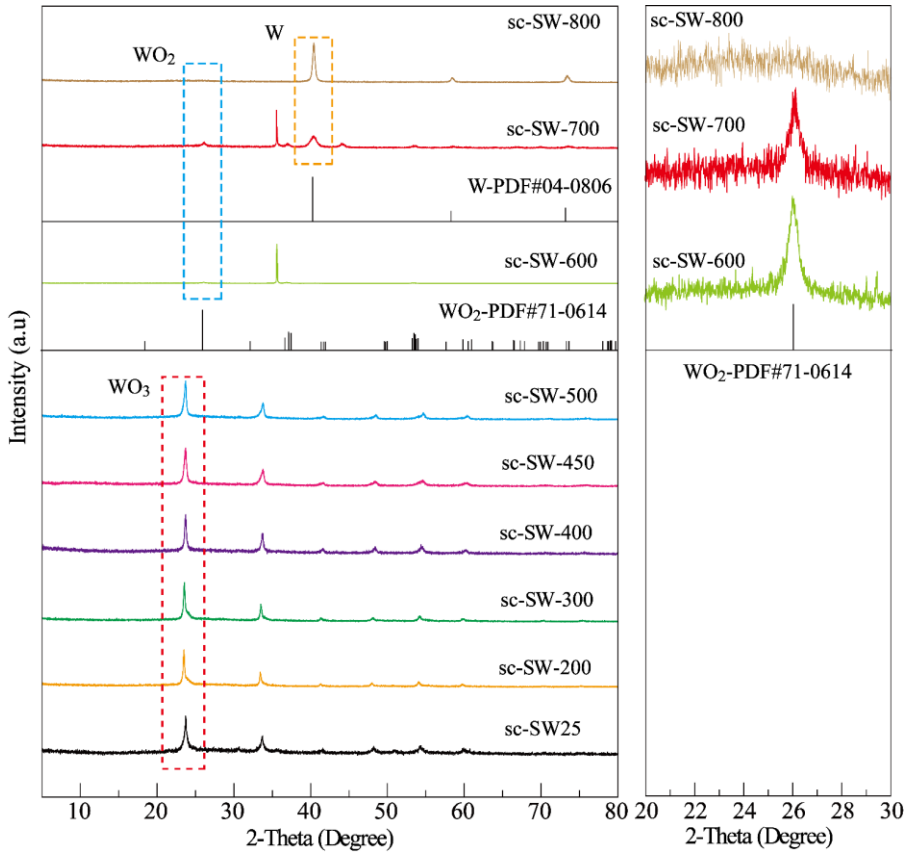

Figure S18. Change of the XRD patterns of single crystal sc-SW-T samples with reduction treating temperature (T) and the corresponding zoom regions.

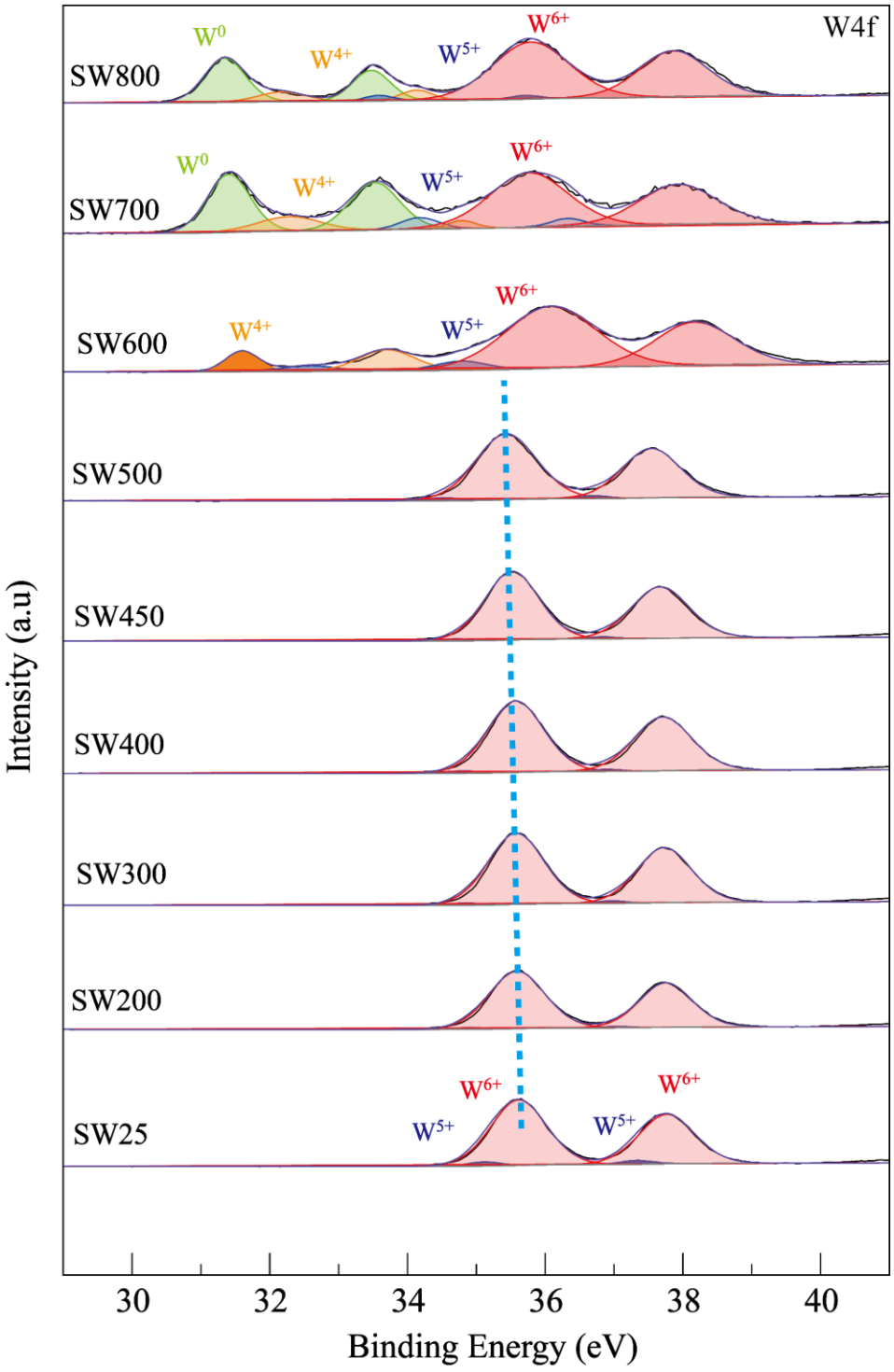

Figure S19. Change of the W 4f XPS spectra of SW-T samples with reduction treating temperature (T).

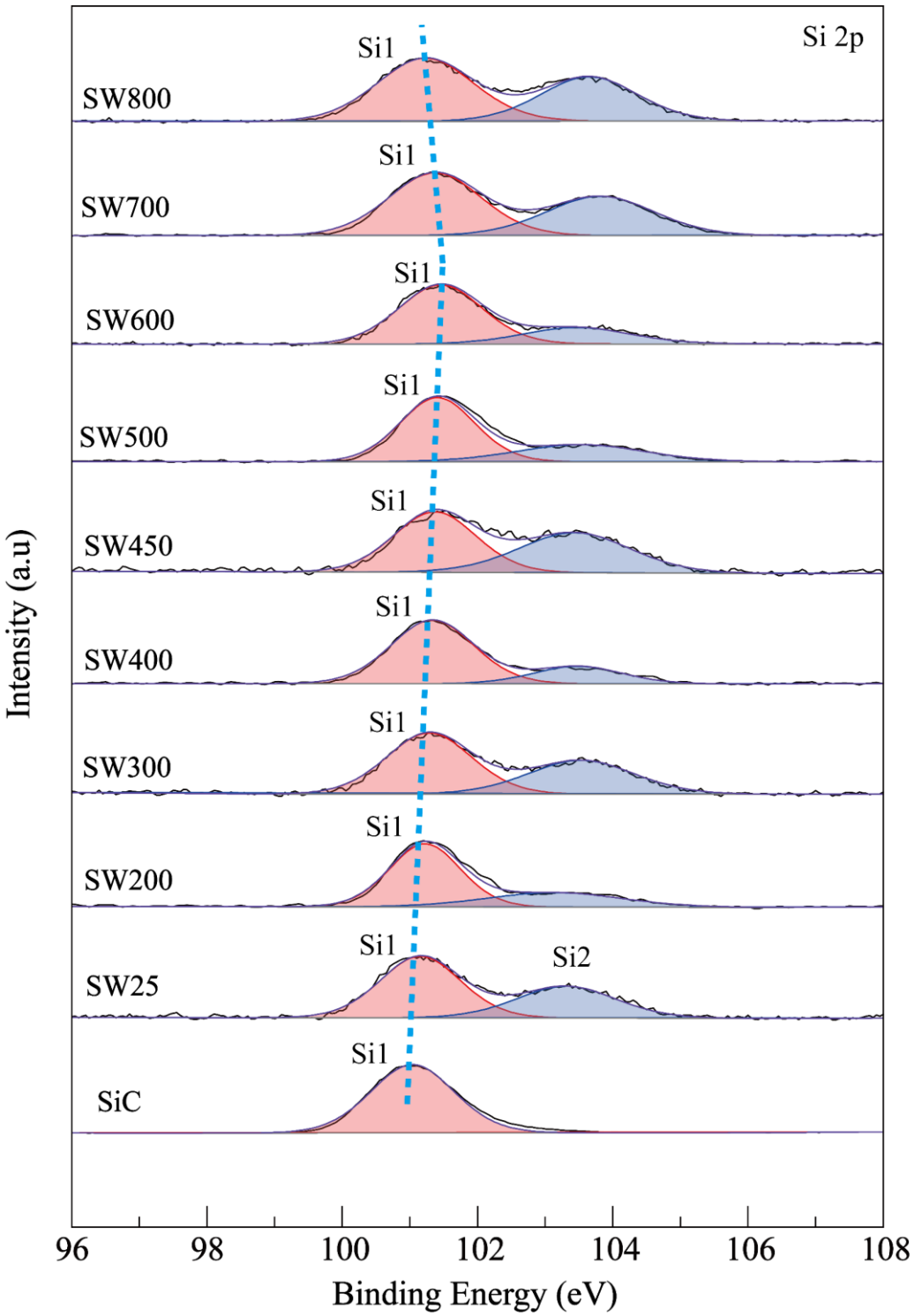

Figure S20. Si 2p XPS spectra of SiC and their changes in SW-T samples with reduction treating temperature.

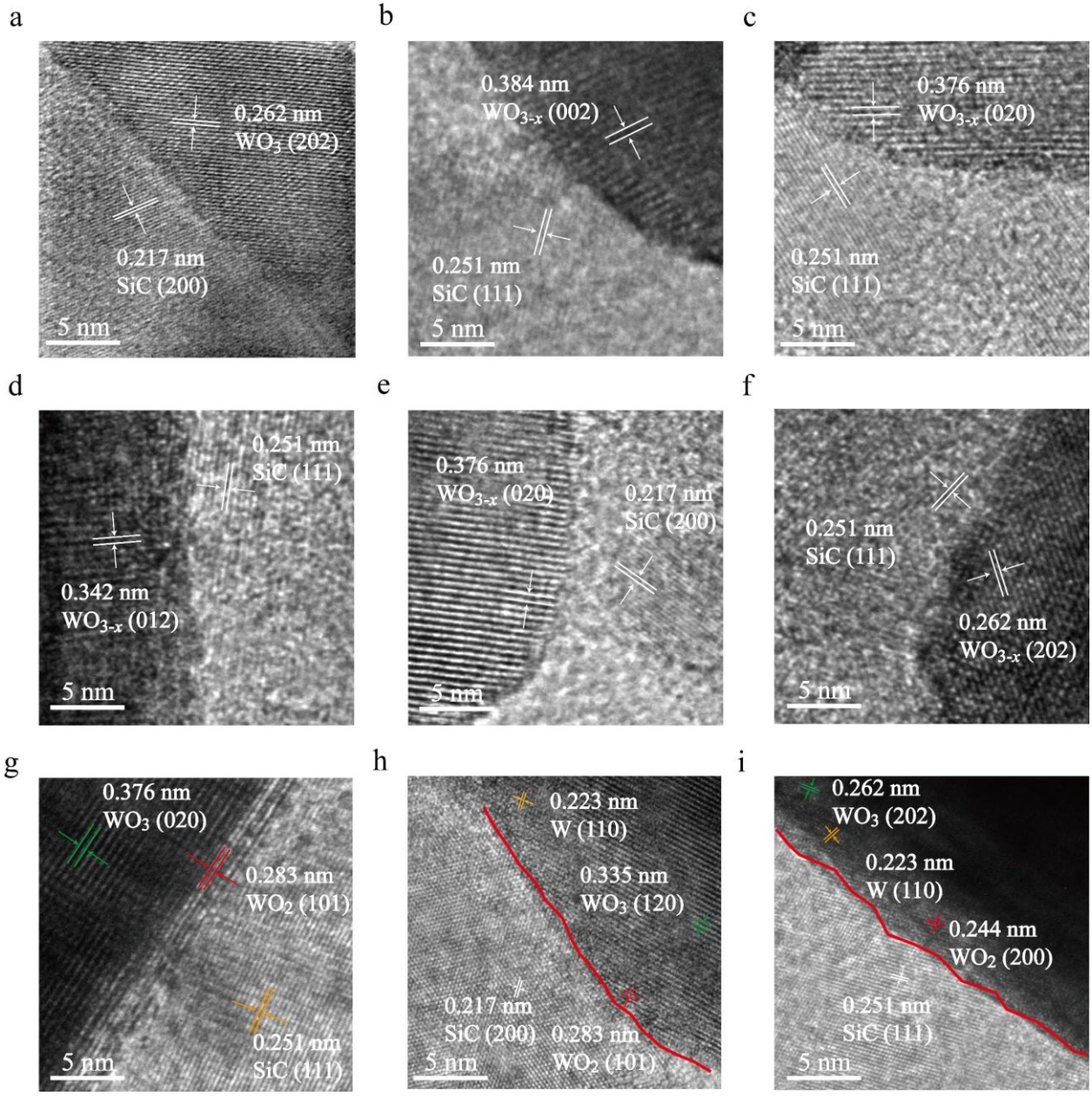

Figure S21. HRTEM images SW-T samples: (a) SW25, (b) SW-200, (c) SW-300, (d) SW-400, (e) SW-450, (f) SW-500, (g) SW-600, (h) SW-700 and (i) SW-800.

Between 200 and 500 °C, SW-T samples retain the heterojunction interface between intimately contacted SiC and WO_{3-x}, as indicated by the relative positions of the lattice fringes (S21a-21f). At 600 °C, the WO_2 phase was observed and closely embedded within the SiC and WO_3 heterojunction interface (S21g). For SW-700 and SW-800 samples, both WO_2 and metal W were found to be closely embedded within the SiC and WO_3 heterojunction interface (S21h-S21i).

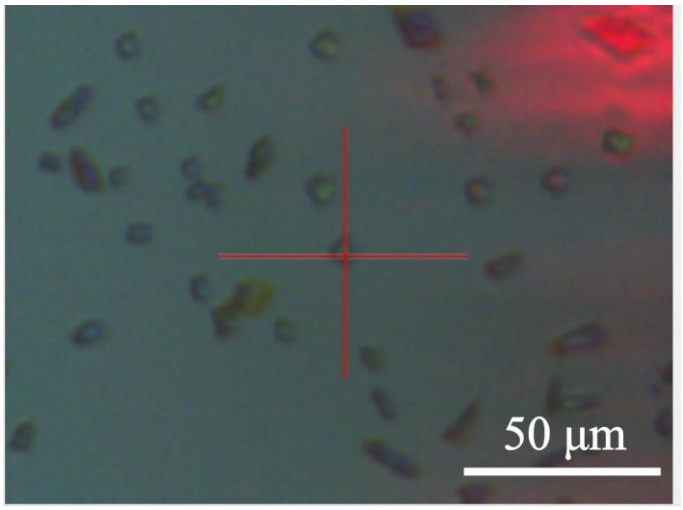

Figure S22. Magnified optical image of the $SiC@WO_3$ sample.

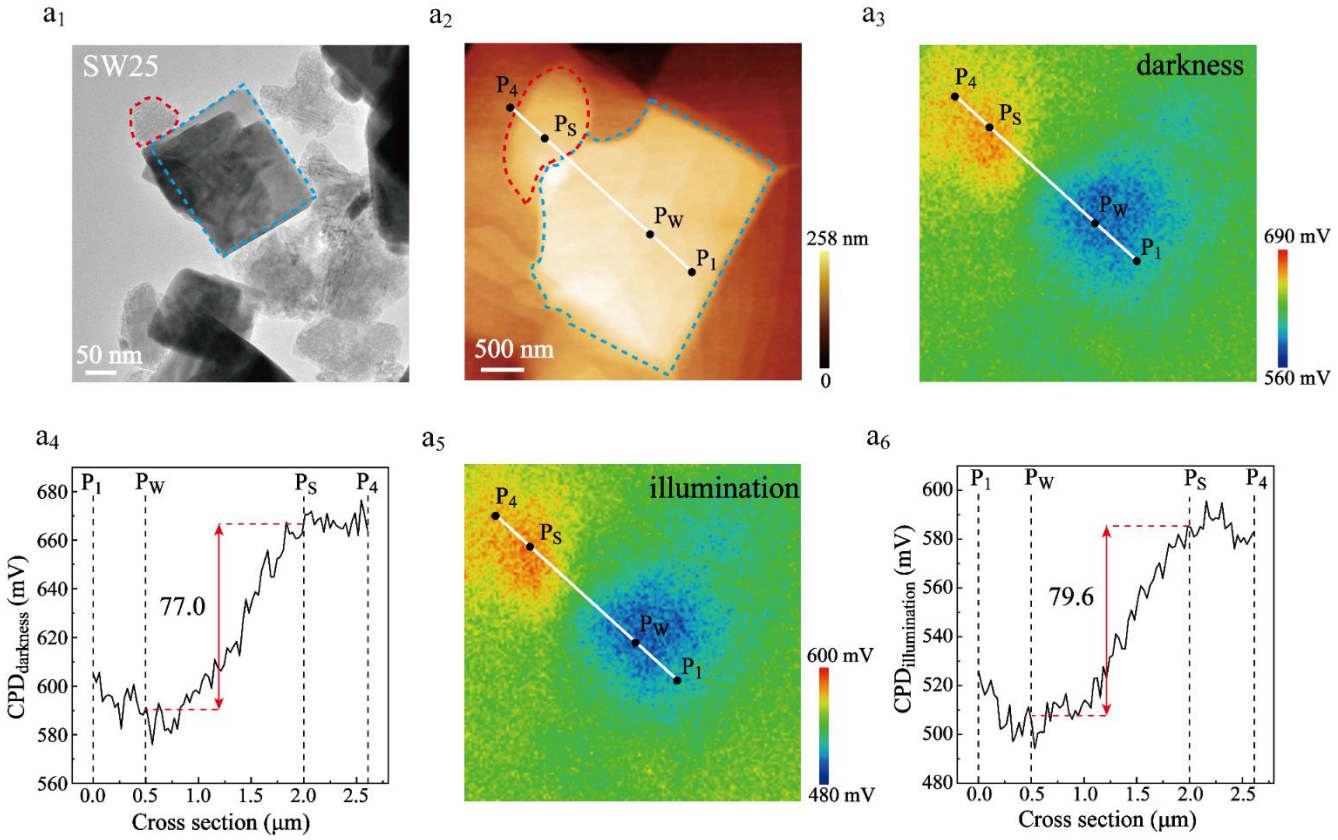

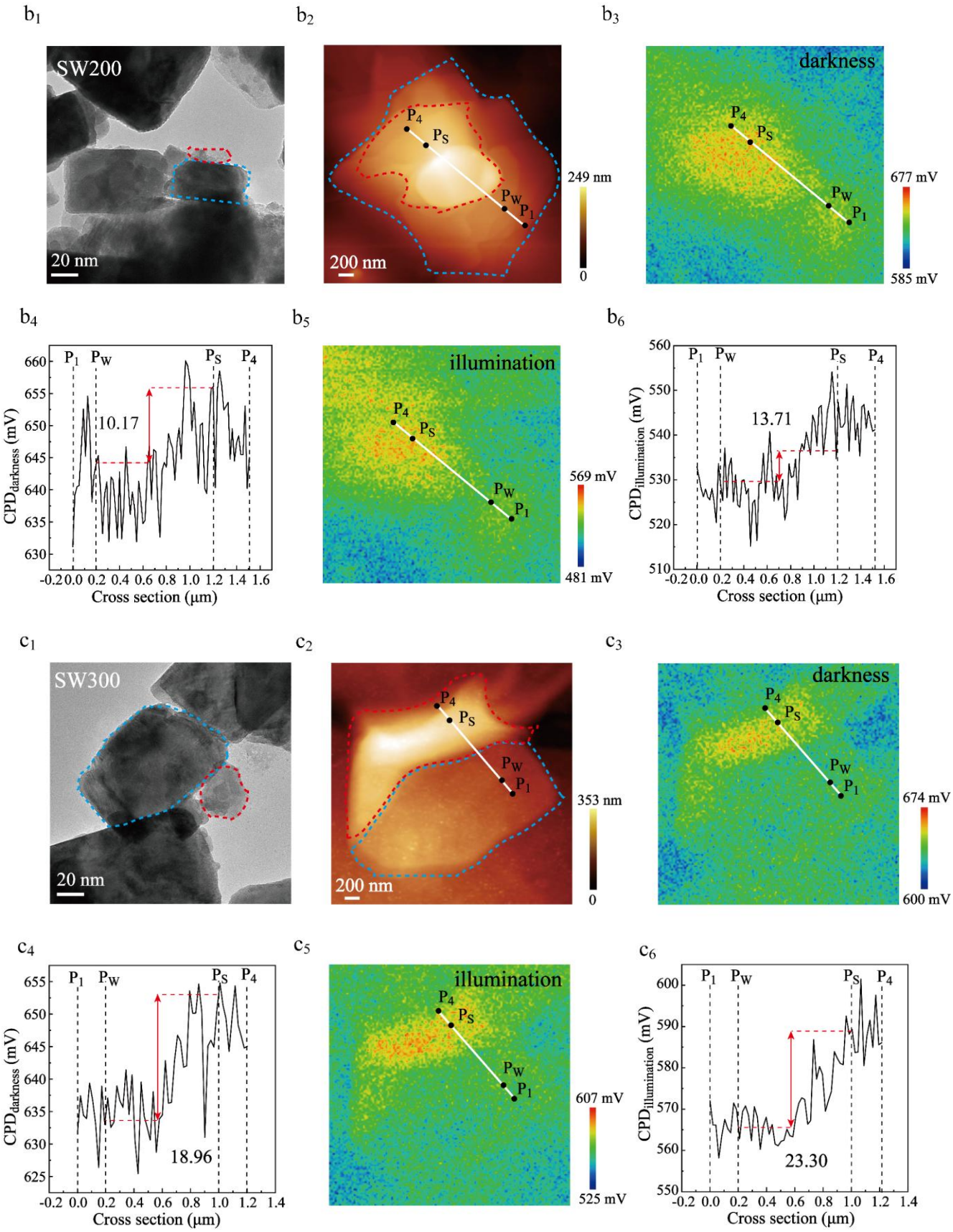
b1
SW200
20 nm
b2
P4
PS
PW
P1
200 nm
249 nm
0
b3
darkness
677 mV
585 mV
b4
P1 PW PS P4
10.17
CPDdarkness (mV)
Cross section (μm)
b5
illumination
569 mV
481 mV
b6
13.71
CPDillumination (mV)
Cross section (μm)
c1
SW300
20 nm
c2
353 nm
0
c3
darkness
674 mV
600 mV
c4
18.96
CPDdarkness (mV)
Cross section (μm)
c5
illumination
607 mV
525 mV
c6
23.30
CPDillumination (mV)
Cross section (μm)

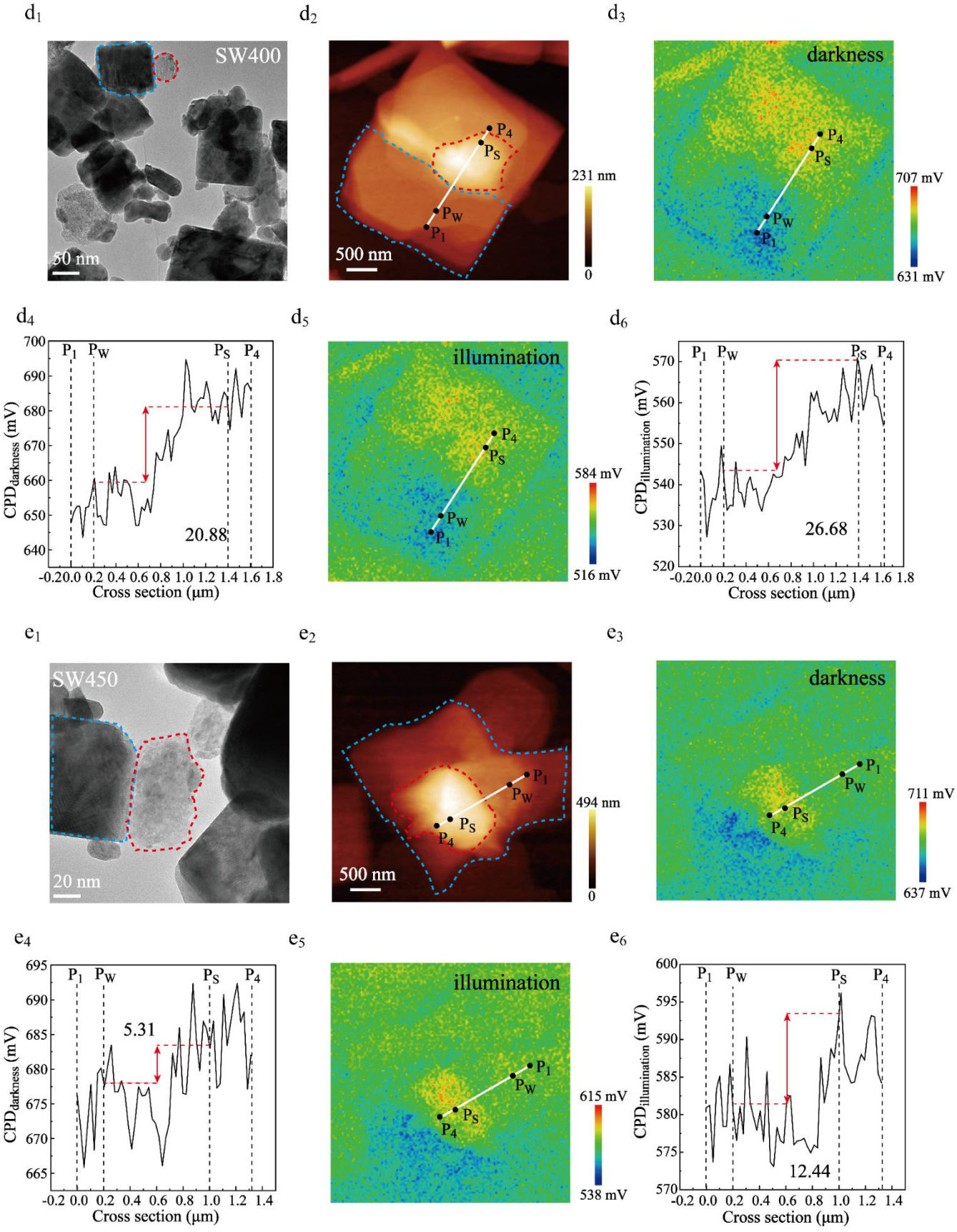
d1
SW400
50 nm
d2
P4
PS
PW
P1
500 nm
231 nm
0
d3
darkness
707 mV
631 mV
d4
P1 PW PS P4
CPDdarkness (mV)
20.88
Cross section (μm)
d5
illumination
584 mV
516 mV
d6
CPDillumination (mV)
26.68
e1
SW450
20 nm
e2
494 nm
e3
711 mV
637 mV
e4
5.31
e5
615 mV
538 mV
e6
12.44

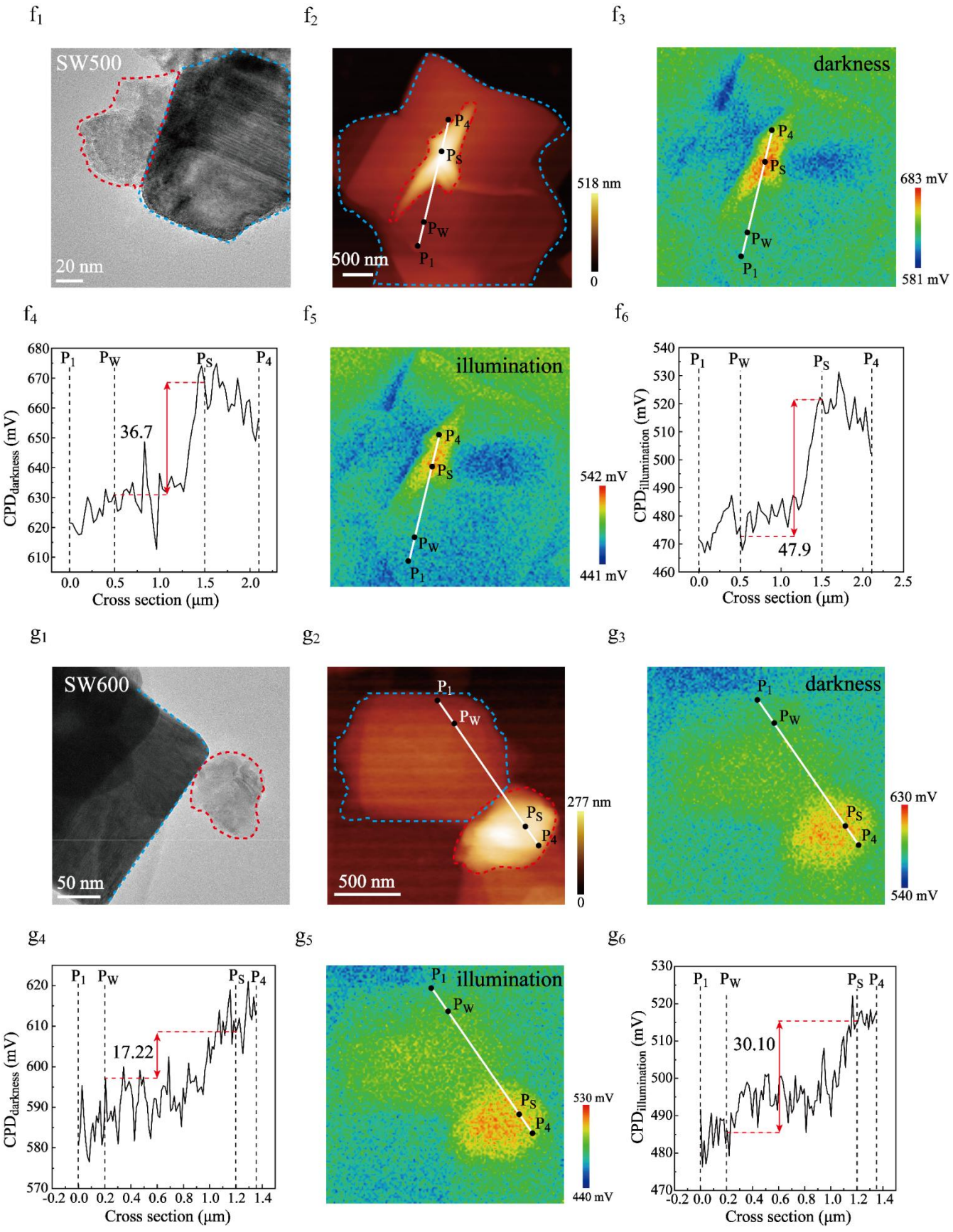
f1
f2
f3
SW500
20 nm
500 nm
518 nm
0
darkness
683 mV
581 mV
P1
PW
PS
P4
f4
f5
f6
CPDdarkness (mV)
Cross section (μm)
36.7
illumination
542 mV
441 mV
CPDillumination (mV)
47.9
g1
g2
g3
SW600
50 nm
277 nm
630 mV
540 mV
g4
g5
g6
17.22
530 mV
440 mV
30.10

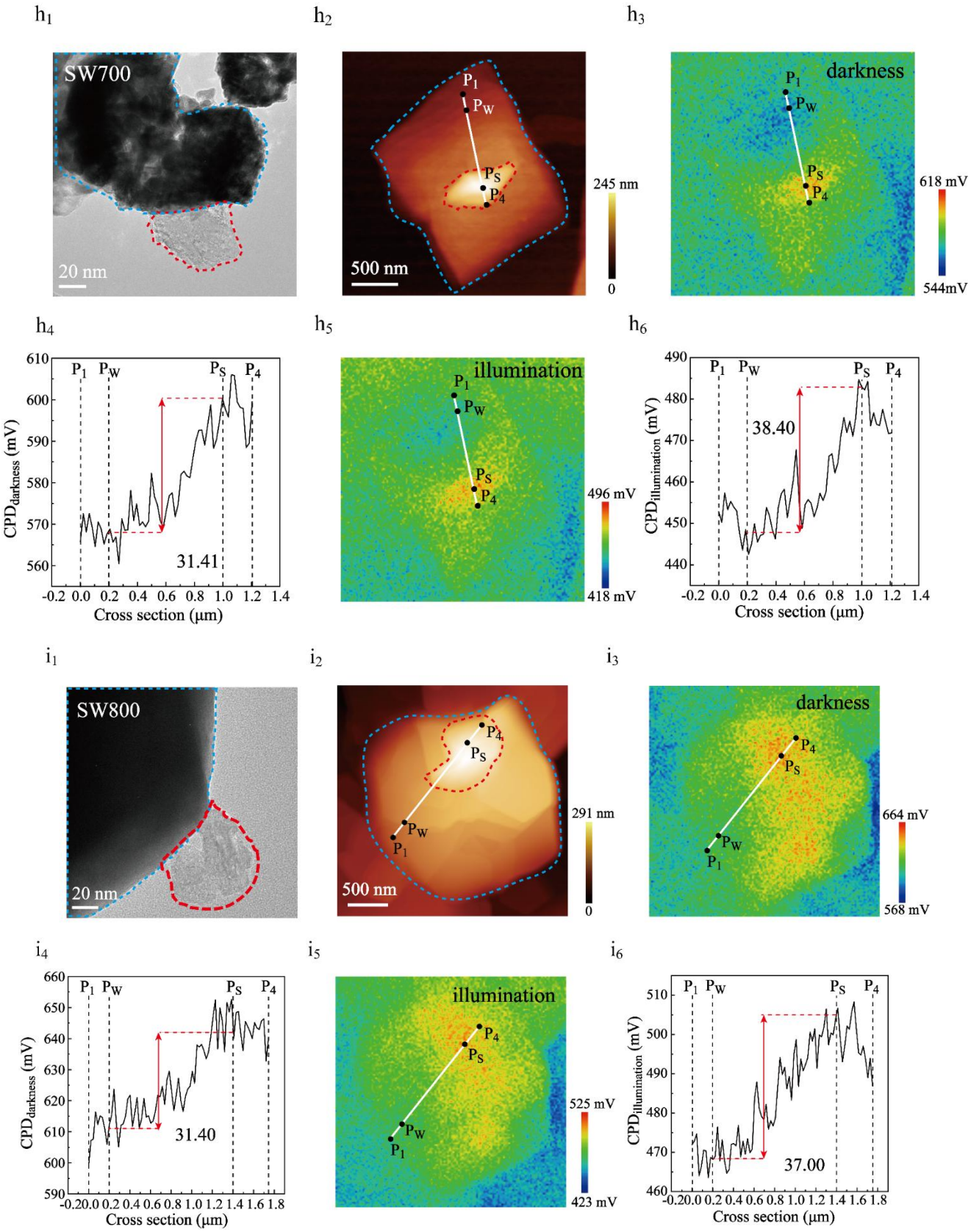

Figure S23. For the SW25 sample and SW-T samples with reduction temperature**:** (a_1-i_1) Change of the TEM images. (a_2-i_2) Change of the topography images. (a_3-i_3) Change of the surface potential distribution images under

darkness. (a_4-i_4) Change of the corresponding surface potential under darkness ($CPD_{darkness}$) along the marked line between P_W (the position of WO_3) and P_S (the position of SiC). (a_5-i_5) Change of the surface potential distribution images under illumination. (a_6-i_6) Change of the corresponding surface potential under illumination ($CPD_{illumination}$) along the marked line between P_W and P_S. The blue dotted circle and red circle denote the region of WO_3 and SiC, respectively.

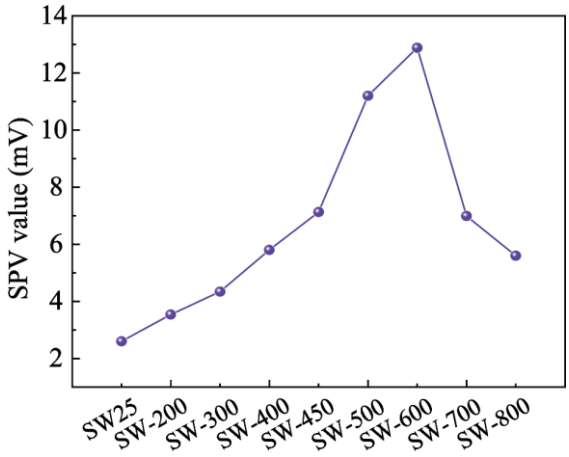

Figure S24. SPV value of SW25 and SW-T samples with reduction temperature.

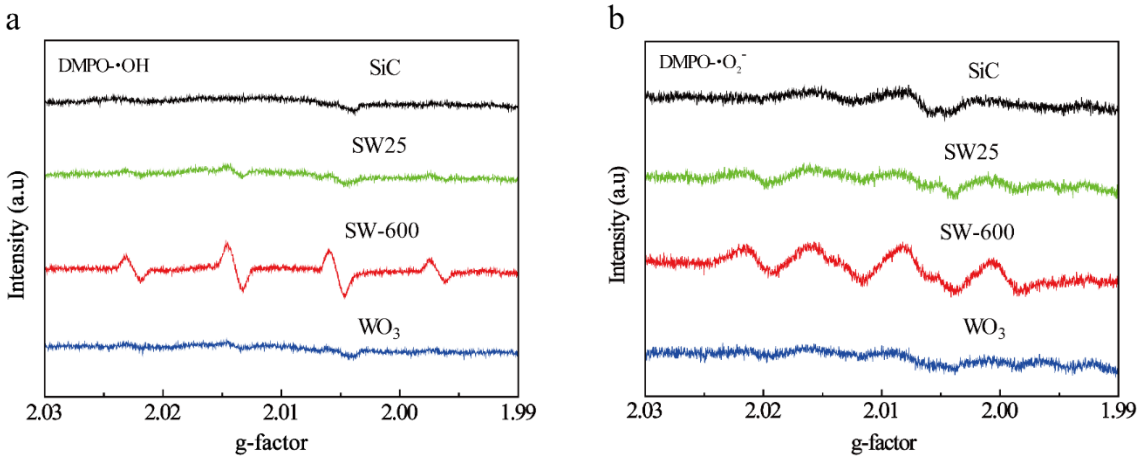

Figure S25. EPR signals of (a) DMPO-·OH and (b) DMPO-·O_2^- of the as-prepared samples under illumination.

Weak EPR signals corresponding to DMPO-·OH were detected in WO_3, and almost no DMPO-·OH signals were seen in the SiC dispersions. It is due to the more negative E_{VB} (+1.47 V) of SiC than the potential of OH^-/·OH (+2.34 V) (S25a) [*Angew. Chem., Int. Ed.* 2022, 61, e202108069.] In comparison, a characteristic EPR signal belonging to DMPO-·OH can be observed in SW25 dispersions, indicating that photogenerated holes of SW25 composite can oxidize the OH^- to ·OH via the valence band of WO_3. Notably, SW-600 shows more distinctive

DMPO-·OH signals than those of SW25. It is possible that the photogenerated holes of SW-600 could be more efficiently separated and migrated to the surface to oxidize the reactants through the valence band of WO_3. In addition, a characteristic EPR signal corresponding to DMPO-·O_2^- was detected in individual SiC. However, almost no distinct DMPO-·O_2^- signals were observed in WO_3. It is due to the comparable E_{CB} (-0.38 V) of WO_3 to the potential of O_2/·O_2^- (-0.33 V). [*Angew. Chem., Int. Ed*. 2022, 61, e202108069.] For the SW25 sample, relatively stronger EPR signals were detected under irradiation, indicating the photogenerated electrons of SW25 can reduce O_2 to ·O_2^- via the conduction band of SiC (S25b). Interestingly, SW-600 exhibits a stronger EPR signal than SW25, which may indicate that its photogenerated electrons on the conduction band of SiC are more effectively transferred to the surface and participate in the reduction reaction.

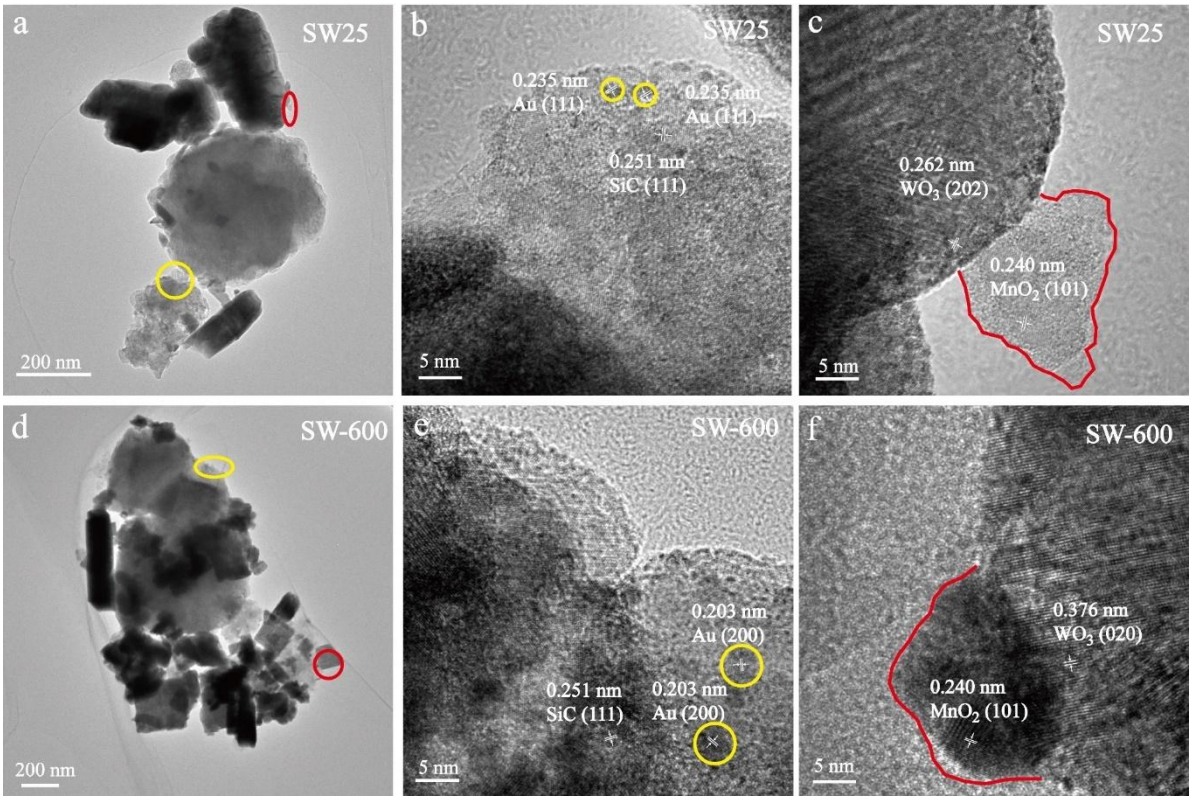

Figure S26. TEM images of samples after the photoinduced redox probe reactions with Mn^{2+} and $[AuCl_4]^-$: SW25 (a) and SW-600 samples (d). HRTEM images of the Au particle distribution (inside the yellow circles) and the MnO_2 particle distribution (inside the red region) on samples: (b) and (c) SW25, (e) and (f) SW-600.

The photoinduced redox probe reactions also demonstrated the above direction of possible electron transfer. For the SW25 sample, Au nanoparticles (inside the yellow circles) are observed to deposit on SiC nanoparticles

(S26b) selectively. From the relative positions of the lattice fringes, *i.e.* the (111) facet of SiC is near the (111) facet of Au. [*J. Phys. Chem. C* 2021, 125, 10964.] In contrast, MnO_2 nanoparticles (inside the red lines) are observed to deposit on WO_3 (S26c) preferentially. The (202) facet of WO_3 is adjacent to the (101) facet of MnO_2. [*J. Phys. Chem. C* 2015, 119, 14834. *J. Hazard. Mater*. 2023, 459, 132199.] These results indicate that SiC and WO_3 serve as the reduction and oxidation sites, respectively, in the photocatalytic reaction on the SW25 sample. After interface modification, this preferred deposition principle can also be observed in the SW-600 sample (S26e-f). For instance, the (111) facet of SiC is close to the (200) facet of Au, and meanwhile, the (020) facet of WO_3 is near the (101) facet of MnO_2. [*Nano Energy* 2016, 24, 94. *J. Catal.* 2019, 372, 8.] It shows photocatalytic oxidation and reduction reactions still selectively occur at WO_3 and SiC in SW-600, correspondingly.

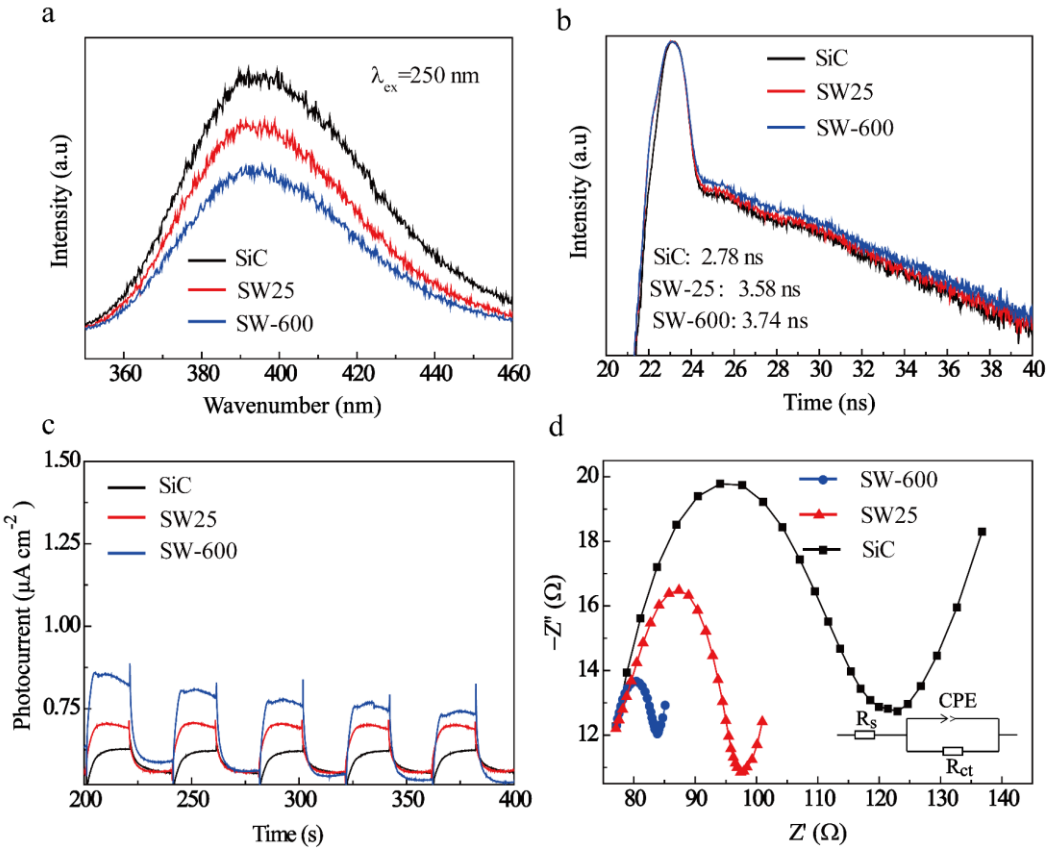

Figure S27. (a) The steady-state Photoluminescence (PL) spectra, (b) transient Photoluminescence (TPL) spectra, (c) the periodic on/off photocurrent response, and (d) EIS plot of SiC, SW25, and SW-600 samples. The bottom right inset (d) is the equivalent Randle circuit. R_s represents the solution resistance; CPE is the constant phase element for the electrode/electrolyte interface; and R_{ct} represents charge transfer resistance across the electrode/electrolyte interface.

Table S1. BET surface area of SW-T samples.

Sample	BET surface area ($m^2 g^{-1}$)	Sample	BET surface area ($m^2 g^{-1}$)
SW25	16.0	SW500	15.1
SW200	17.8	SW600	16.2
SW300	16.5	SW700	12.1
SW400	15.5	SW800	13.7
SW450	16.1		

Table S2. Electronic structure parameters of SiC and WO_3.

Sample	SiC	WO_3
E_{VB} vs vacuum energy level (eV)	-5.91	-6.81
E_{CB} vs vacuum energy level (eV)	-3.43	-4.03
E_{VB} vs RHE (V)	1.47	2.37
E_{CB} vs RHE (V)	-1.01	-0.41
Bandgap (E_g)	2.48	2.78
Work function (eV)	4.0[a)]	5.05[a)]

[a)] The work function value of SiC and WO_3 is referred to. [*J. Mater. Chem*. 2008, 18, 509] and [*Sens. Actuators, B* 2013, 187, 379.]